



1 **Influence of the previous North Atlantic Oscillation (NAO)**
2 **on the spring dust aerosols over North China**

3 **Yan Li¹, Falei Xu¹, Juan Feng², Mengying Du¹, Wenjun Song¹, Chao Li^{1,3}, and Wenjing**
4 **Zhao^{1,4}**

5 ¹Key Laboratory for Semi-Arid Climate Change of the Ministry of Education, College of
6 Atmospheric Sciences, Lanzhou University, Lanzhou, China

7 ²College of Global Change and Earth System Science, Beijing Normal University, Beijing, China

8 ³Hubei Key Laboratory for Heavy Rain Monitoring and Warning Research, Institute of Heavy
9 Rain, China Meteorological Administration, Wuhan, China

10 ⁴Gansu Meteorological Service Center, Lanzhou, China

11 **Correspondence:** Juan Feng (fengjuan@bnu.edu.cn)

12

13 **Abstract.** The North Atlantic Oscillation (NAO) has been confirmed to be closely related to the
14 weather-climate in many regions of the Northern Hemisphere, however, its effect and mechanism
15 upon the formation of regional dust events (DEs) have rarely been involved in China. By using the
16 station observation data, and multi reanalysis datasets, the influence of NAO on the dust aerosols
17 (DAs) in China, as well as the corresponding mechanism of synoptic cause are explored in
18 perspective of transient eddy fluxes. It is found that the DAs in the non-dust source areas show high
19 values with a strong annual variability in north of the Yangtze River (30-40°N, 105-120°E), which
20 is referred to as the North China hereafter. A significant negative relationship is indicated between
21 the boreal winter NAO index and the late spring DAs in the North China with the correlation
22 coefficient of -0.39. According to the 9 spring DEs affected significantly by negative phase of the
23 preceding winter NAO in the North China during 1980-2020, it is shown that before the outbreak
24 of DEs, due to the transient eddy momentum (heat) convergence (divergence) over the dust aerosol
25 (DA) source regions, the zonal wind speed increases in upper-level troposphere, strengthening the
26 zonal wind in the middle-lower levels through momentum downward transmission. Simultaneously,
27 there is transient eddy momentum (heat) divergence (convergence) around the Ural Mountains,
28 which is favorable for establishment and maintenance of the Ural ridge, as well as development of
29 the air temperature and vorticity advections. The combined action of temperature and vorticity



30 advections results in the Siberian Highs and Mongolian cyclone to establish, strengthen, and move
31 southward near the surface, guiding the cold air from high latitudes southward, and is favorable to
32 the uplift and transmission of DAs to the downstream North China. After the outbreak of DEs,
33 change of transient eddy fluxes in the DA source regions and the Urals regions, leads to both energy
34 and mass divergence and reduction of the zonal winds over the North China. Accompanying with
35 the prevailing southerly airflow in south of the North China, a stable high value of DA concentration
36 is maintained for 1-2 days. This study reveals the impact of transient eddy fluxes transport on the
37 dusty weather anomalies modulated by the NAO negative signal in the North China, which can
38 deepen the understanding of formation mechanism of DEs in China.

39

40 **1 Introduction**

41 Airborne dust aerosols (DAs), which play a significant role in the evolution of the atmospheric
42 system, have an important influence on human society, ecosystems, and biochemical cycles. In
43 particular, the radiative forcing of DAs is comparable to that of clouds on a regional-scale and has
44 a key impact on the local weather-climate (Kaufman et al., 2002; Huang et al., 2014a). Recently,
45 the influence of DAs on the weather-climate has attracted widespread attention from researchers,
46 and the direct, indirect and semi-direct feedback responses between them have been confirmed by
47 scientific studies. For direct processes, DAs can impact the weather-climate by scattering shortwave
48 and longwave radiation to cool the atmosphere or by absorbing longwave radiation and solar
49 shortwave radiation released by the earth and clouds to heat the atmosphere (Sokolik and Toon,
50 1996; Zhang et al., 2019); via indirect influence, DAs can change the local rainfall processes as well
51 as the albedo of ice and snow surfaces by altering the characteristics of cloud condensation nuclei
52 and ice nuclei (Ackerman et al., 2000; Sassen et al., 2003); and in the semi-direct effects, DAs can
53 increase cloud droplet evaporation and reduce cloud water pathways by heating the clouds (Huang
54 et al., 2006). In addition, it has been found that due to the increase of DAs in the Arabian Sea,
55 Arabian Peninsula, and West Asia, the Indian summer monsoon will be enhanced and thus influence
56 the rainfall in central India (Jin et al., 2016). The DAs of worldwide annual emissions in the range
57 of 1000-2150 Tg are lifted up by the surface wind (Zender et al., 2004), with only approximately
58 30% of these resettle in the dust aerosol (DA) source regions, while the other 70% is transported



59 to downstream areas thousands of kilometres away, causing changes in the local weather-climate
60 (Duce et al., 1980; Huang et al., 2015).

61 One of the most serious natural catastrophes in East Asia is dusty weather. Studying the
62 climatological features, variations, and influencing factors of DAs are crucial to both understanding
63 and predicting DA variation patterns (Feng et al., 2020; Yao et al., 2021). Extensive analysis of
64 meteorological and climatic factors associated with the occurrence of global dust events (DEs) have
65 been conducted using ground-based observations (e.g., Ji and Fan, 2019; Liu et al., 2020), satellite
66 remote sensing (e.g., Chiapello et al., 2005; Han et al., 2022), and numerical simulations (e.g.,
67 Ginoux et al., 2004; Chen et al., 2017). It is concluded that the variations in DA concentration and
68 transport are related to many factors, including atmospheric circulation (Huang et al., 2021), surface
69 wind (Liu et al., 2004; Wang et al., 2018), cyclone frequency (Yu et al., 2019), Asian monsoon
70 (Wilcox et al., 2020), and the North Atlantic Oscillation (NAO) (Mao et al., 2011; Li et al., 2019;
71 Feng et al., 2019). The deserts in northern and western China and Mongolia are the most important
72 areas affecting China (primarily Badain Juran and Taklimakan), and the DAs in the above source
73 areas contribute 70% of the dust emissions in East Asia (Zhang et al., 2003; Che et al., 2019).
74 Therefore, it is of great significance to explore the characteristics and causes of DAs.

75 According to previous studies, spring is the most active time for the occurrence of DEs in
76 China, accounting for over 80% of all DEs yearly (Liu et al., 2004). According to statistical analysis,
77 the annual dust emissions in northern China are approximately 25 Tg, of which spring emissions
78 account for over half (Xuan et al., 2000). Recently, DEs seem to be frequent in China, seriously
79 endangering human health, hindering socioeconomic development and causing widespread concern
80 among the scientific community and the public. For example, from 14-16 March 2021, a large-scale
81 dust event (DE) occurred in northern China (Yin et al., 2021), resulting in more than 3.8 million
82 km² affected, with the maximum hourly average concentration of PM₁₀ surpassing 8000 μm^{-3} and
83 a drop in visibility to less than 0.5 km in Beijing (Zhang et al., 2022). In addition, approximately
84 800 Tg of DAs in China are emitted into the atmosphere every year, nearly half of the global
85 emissions (Zhang et al., 1997). Therefore, it is of important practical and scientific value and
86 relevance to investigate the formation mechanism of DEs in China, especially in spring.

87 In the Northern Hemisphere (NH), the NAO is a seesaw mode of centre pressure variation



88 (Walker, 1924) near the Azores and Iceland, and is the most important low-frequency dipole pattern
89 during boreal winter. The NAO has crucial effects on temperature (e.g., Hurrell, 1995; Yu et al.,
90 2016), precipitation (e.g., Hartley and Keables, 1998; Giannini et al., 2000), and storm tracks (e.g.,
91 Lau and Nath, 1991; Jin et al., 2006) in the North Atlantic and its surrounding areas. However, its
92 signal can also be used as a mediator waveguide through the midlatitude westerly wind belts,
93 capturing the downstream propagating Rossby wave train and thus extending its effect to the
94 weather-climate of the Eurasian continent, as well as the entire NH (e.g., Watanabe, 2004; Lin et al.,
95 2011; Zhang et al., 2021). China is located downstream of the NAO-connected circulation system,
96 and its climate is impacted by variations in different phases and intensities of the NAO. For example,
97 when the NAO is unusually strong in winter, China will be controlled by an abnormally warm and
98 rainy climate during the same period, and the temperature in the Yangtze-Huaihe River Basin will
99 be abnormally cooler in the next summer (Wang and Shi, 2001). Liu et al. (2001) found that changes
100 in the NAO can alter the temporal and spatial distributions of precipitation in the eastern Tibetan
101 Plateau in summer by affecting the tropospheric zonal winds. The NAO also has a key influence on
102 weather-scale anomalies in China. Li et al. (2021a) explored the connection between the NAO and
103 persistent haze events in Beijing and found that the NAO negative signal can modulate wave train
104 transmission to northern China, exacerbating the haze duration in Beijing. Yao et al. (2022) indicated
105 that under the influence of seasonal accumulation of the NAO negative signal, the polar vortex will
106 become more vulnerable and unstable compared to the climatic mean value, which will lead to more
107 extreme cold occurrences in China.

108 Meanwhile, it has been shown that the NAO also has a crucial influence on the process of DEs
109 in China. For example, Tang et al. (2005) noted that the frequency of spring DEs in northern China
110 was significantly influenced by fluctuations in the NAO intensity. In addition, Zhao et al. (2012)
111 discovered an obvious negative correlation between the winter NAO intensity and the late spring
112 and summer DEs in northwestern China. The above studies mainly analysed the association between
113 the NAO and the DEs in China from the perspective of seasonal-scale climate. However, the
114 influence of weather-scale meteorological elements on DEs is also important. For example, Qian et
115 al. (2002) explored the connection between Chinese DEs and cyclonic activities from 1948 to 1999
116 and found a highly positive correlation between them. Wang et al. (2009) further discovered that the



117 spring DEs in northern China were mostly near the centre of the Mongolian Cyclone (MC). Hara et
118 al. (2006) used a regional-scale DA transport model and found that the frequency of DEs in the Gobi
119 Desert of East Asia can also be increased by the intrusion of polar cold air. Furthermore, An et al.
120 (2018) discovered that the decline in the strength and frequency of DEs in East Asia during the
121 period of 2007-2016 was highly associated with the weakening tendency of strong winds following
122 the entrance of higher-latitude cold air. As mentioned previously, the large-scale climate variability
123 model of the NAO can capture the Rossby wave train propagating downstream, which in turn has a
124 crucial effect on the weather-scale elements. As one of the two fundamental fluctuations in the
125 atmosphere, transient eddy is widely used in studies to diagnose Rossby wave trains (Trenberth,
126 1986) and can provide a perspective of mechanism exploration in abnormal variations in
127 atmospheric circulation (Li et al., 2022). It has been noted that transient eddy has a sustained impact
128 on the development of atmospheric systems such as the Siberian Highs (SH) as well as the North
129 Pacific low. (Holopainen and Oort, 1981; Holopainen et al., 1982). The forcing impact of transient
130 eddy on the mean airflow can enhance anticyclonic circulation, which in turn may trigger large-
131 scale severe low-temperature occurrences (Li et al., 2019b). In addition, Li et al. (2022) showed that
132 transient eddy played a significant role in the formation of abnormal atmospheric circulation of DEs
133 by focusing on the spring DEs in south Xinjiang, China, during 1980-2018.

134 It is essential to continue deep study of the synoptic mechanism of DE formation through the
135 aspect of the NAO. On the one hand, with the recent huge energy consumption and astounding
136 economic development in East Asia, the eastern part of China has suffered from escalating air
137 pollution problems (Zhang et al., 2012; Zhao et al., 2016). With the occurrence of DEs, DAs are one
138 of the most crucial elements affecting air quality in East Asia (Huang et al., 2014b; Nie et al., 2015).
139 Previous studies have provided some analysis and initial progress on the relationship between the
140 NAO and the DEs in northern China regions, mainly DA source areas such as northwestern China.
141 However, such studies are limited to the eastern part of China, which is not a DA source area but is
142 severely affected by DEs. On the other hand, previous studies of the NAO on the DEs in China have
143 mainly been analysed on the seasonal-scale to provide a large-scale climatic background for the
144 occurrence of DEs in China, but it is not clear how the NAO affects the DEs in China at the synoptic-
145 scale, and the role of transient eddy in the anomalous circulation of the atmosphere in DEs under



146 the modulation of the NAO is uncertain.

147 From the above points of view, we investigated three main scientific questions in this paper: 1)
148 Does the NAO affect the area with high values of DAs in eastern China? What are the characteristics
149 of the impact? 2) What are the synoptic causes of the formation of DEs influenced by the NAO? 3)
150 How can we explain the mechanism of the formation of synoptic system anomalies by transient
151 eddy under NAO modulation? To address the above issues, by using station observation data, the
152 MERRA-2 dataset, and reanalysis datasets from 1980-2020, this paper investigated the long-term
153 changes in the spring DAs in China to examine the characteristics of the impact of NAO on the DAs
154 in eastern China during the previous period and the same period, and to explore the atmospheric
155 circulation mechanisms affecting DEs considering transient eddy flux transport under the influence
156 of the NAO. The remaining work is organized as follows. Section 2 describes the datasets and
157 methods employed in this paper. Sections 3.1, 3.2, and 3.3 cover the selection of DA study area and
158 its link with the NAO, the process of abnormal atmospheric circulation during DEs, and the impacts
159 of the transport features of transient eddy fluxes accompanying synoptic system anomalies,
160 respectively. Section 4 contains the conclusions and discussions.

161

162 **2 Datasets and methods**

163 **2.1 Datasets**

164 The China National Meteorological Center (CNMC) provides the daily DE occurrence dataset
165 over mainland China, which contains three types of DEs (dust storm, blowing dust, and floating
166 dust). When DAs are transported with visibility less than 1 km, it is considered a dust storm, whereas
167 floating dust with visibility less than 10 km is caused by DAs from upwind source regions, and
168 blowing dust is defined similarly to floating dust, with the difference that the DAs are emitted from
169 local source areas. Several previous studies have confirmed the validity of the dataset (Kang et al.,
170 2016; Wang et al., 2018).

171 Datasets of daily and monthly DA concentrations under the Modern-Era Retrospective
172 Analysis for Research and Applications, version 2 (MERRA-2), were derived from the Global
173 Modeling and Assimilation Office (GMAO) of the National Aeronautics and Space Administration
174 (NASA) (Gelaro et al., 2017). Its foundation is built on the assimilation of multiple satellite systems



175 (AVHRR, MISR, MODIS) and AERONET ground-based observations, and the correctness and
176 reliability are considered to be better than those obtained from the assimilation of individual
177 satellites. The MERRA-2 DA dataset is used for the Goddard Earth Observing System Model,
178 version 5 (GEO-5) (Molod et al., 2015) and the grid statistical interpolation analysis method for
179 three-dimensional variable assimilation (3DVar) (Kleist et al., 2009). The most significant benefit
180 of the MERRA-2 dataset is the temporal and spatial coherence, which cannot be surpassed by
181 station-based or individual satellite data and allow for rigorous statistical analysis of the temporal
182 and spatial patterns (Gelaro et al., 2017). The dust column mass density was used to represent the
183 atmospheric DA concentration under the MERRA-2 product during the 1980-2020 period
184 (horizontal resolution: $0.625^\circ \times 0.5^\circ$) in this paper. Yao et al. (2021) used the MERRA-2 dataset to
185 analyse the monthly mean DAs in China and found that the DAs from March to July showed higher
186 values with obvious variabilities, which was consistent with the previous conclusions obtained using
187 different DA datasets (Che et al., 2019; Liu et al., 2020), demonstrating the feasibility and
188 applicability of the MERRA-2 dataset for assessing the DAs in China.

189 The Sea Surface Temperature (SST) dataset was obtained from the Extended Reconstructed
190 Sea Surface Temperature, version 5 (ERSST-5), from the National Oceanic and Atmospheric
191 Administration (NOAA) for the period 1980-2020 (horizontal resolution: $2.0^\circ \times 2.0^\circ$) (Huang et al.,
192 2017). The atmospheric reanalysis datasets, including the wind field, geopotential height field, sea
193 level pressure field, temperature field, and vertical velocity field, were obtained from the European
194 Center for Medium-Range Weather Forecasts, version 5 (ERA-5), over the period 1980-2020
195 (horizontal resolution: $0.25^\circ \times 0.25^\circ$). Compared to its predecessor, ERA-Interim, ERA5 has a
196 modified data assimilation system and improved physical model to achieve reanalysis data
197 information with improved quality.

198 In this paper, unless otherwise specified, the boreal winter season is referred to as December-
199 January-February (DJF), and the spring season is March-April-May (MAM).

200

201 **2.2 Methods**

202 The NAO index (NAOI) was chosen to indicate the NAO activities. The NAOI describes the
203 large-scale circulation characteristics of the NAO well (Li and Wang, 2003), and is defined by the



204 following equation:

$$205 \quad NAOI = \hat{P}_{35^{\circ}N} - \hat{P}_{65^{\circ}N} \quad (1)$$

206 In the above equation, P represents the monthly mean sea level pressure averaged from
207 $80^{\circ}W$ to $30^{\circ}E$, \hat{P} is the standardized value of P , and the subscript \hat{P} indicates the latitude.
208 The selection criteria for the NAO abnormal years are based on the NAOI index averaged over the
209 winter months, the index is then normalized, and the years with a NAOI exceeding 0.5 standard
210 deviations are recorded as NAO anomalous years.

211 According to the operational criteria of the CNMC, DE occurrences are defined as when the
212 number of sites with DEs is more than 1/3 of the total amount in the selected region. According to
213 the variations in DAs and to assure the feasibility of DE sample number, we defined a DE when any
214 of three types of DEs occur. Although the DEs last for a short period of time, even only one day, the
215 abnormal atmospheric circulation that affects the DEs will exist over a long period before and after
216 the day of the outbreak of DEs (Li et al., 2022). Therefore, to investigate the abnormal atmospheric
217 signals during DEs, the time-scale was separated into the following parts: “Day -n”, “Day 0” and
218 “Day +n”, which indicate previous to, the date of, and lag after the day of DE outbreak, respectively.
219 To probe obvious signals in DEs, we extended the number of days of DE cycle to 6 days, i.e., before
220 the DE outbreak to “Day -3” and after the DE outbreak to “Day +2”.

221 To analyse the features of transient eddy flux transport during DEs based on atmospheric
222 variables, the method of physical decomposition was used in this work (Qian, 2012). Any
223 atmospheric element F , such as u , v , and T , can be decomposed into two parts according to the
224 above decomposition principle: the temporal mean part \bar{F} and the transient eddy part F' . \bar{F}
225 represents the state in which the radiation from the subsurface at a fixed point in the atmosphere is
226 in equilibrium with the daily and annual cycles of solar radiation, while F' is a deviation from
227 the balanced state as follows:

$$228 \quad F = \bar{F} + F' \quad (2)$$

229 In this paper, the transient eddy flux transport is denoted by $[u'v']$ and $[v'T']$, representing
230 the momentum and heat of transient eddy transport, respectively. Within the range of longitude that
231 we choose, the zonal means are represented in the variables by square brackets $([\])$.

232

233

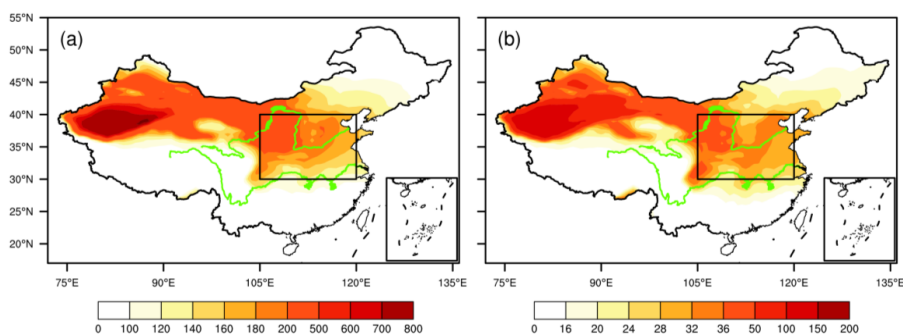


234 3 Results

235 3.1 Selection of the dust aerosol study area and association with the NAO

236 The concentration of spring DA and their standard deviation distributions in China are shown
237 in Fig. 1. The large values of DAs are mostly situated in source regions such as Xinjiang and Inner
238 Mongolia. In addition, the DA concentrations in the non-dust source areas north of the Yangtze
239 River (30–40°N, 105–120°E) also show high values (Fig. 1a); that is, the spring DAs show higher
240 concentrations here than in other regions of China. Moreover, the standard deviation of DAs in this
241 region is also characterized as a large value, indicating that DAs have strong annual variability and
242 are easily influenced by dust disasters (Fig. 1b). Therefore, the area spanning (30–40°N, 105–120°E)
243 is selected as the study region to explore the variability of DAs and the possible formation causes
244 of DEs, which in the analysis that follows is referred to as North China.

245



246

247 Figure 1. Spatial distribution of the climatologically averaged dust column mass density (a) and dust
248 column mass density standard deviation (b) in spring during 1980–2020, unit: mg m^{-2} . The black
249 box indicates the North China study area.

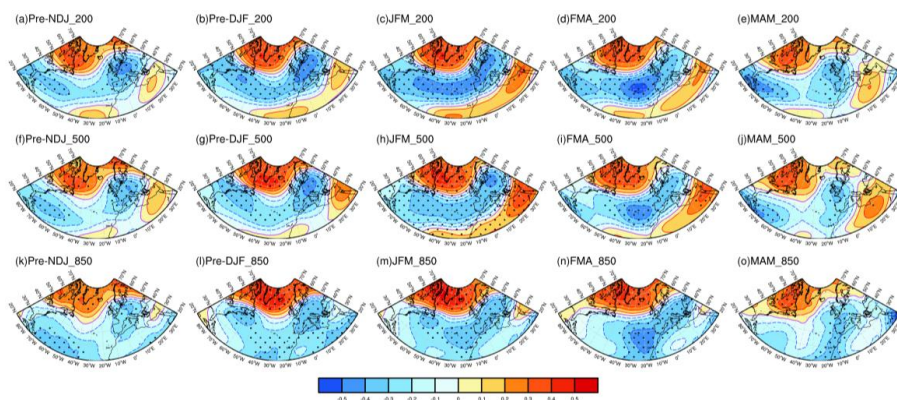
250

251 To explore the possible links affecting the spring DAs in North China, the correlation
252 coefficients between the regional average DAs and the geopotential height field are illustrated in
253 the previous and contemporaneous periods (Fig. 2). The pattern of the MAM DAs and the DJF, JFM,
254 FMA and MAM geopotential height fields all show significant north–south reversal in the North
255 Atlantic, i.e., negative in the Azores and positive in Iceland, which indicates typical characteristics
256 of the NAO negative phase. This dipole structure can be observed in the lower, middle and upper



257 troposphere, denoting that there is an important connection between the spring DAs in North China
258 and the previous NAO variations. Furthermore, significant correlation coefficients can be found
259 between the spring DAs in North China and the NAOI in DJF, JFM, and FMA in the early period,
260 and the correlation coefficients are all approximately -0.40. Simultaneously, as illustrated in Fig. 3,
261 March, April and May, corresponding to the spring months, show substantial standard deviations,
262 suggesting that the DAs in North China vary dramatically in these 3 months, while the monthly
263 average standard deviations of the NAOI present the highest values in December, January and
264 February, corresponding to the winter. Therefore, the effect of the NAO in boreal winter on the later
265 spring DAs in North China and the synoptic formation mechanism of the impact should be analysed
266 and explored. Considering the significant negative effect of the NAO on the DAs in North China,
267 the main focus in the subsequent analysis is on the negative phase of the NAO.

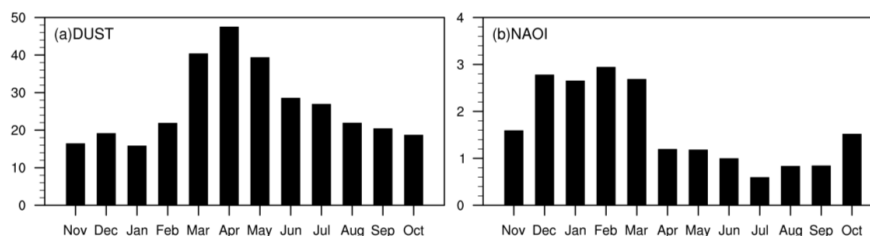
268



269

270 Figure 2. Correlations of the spring dust column mass density in North China from 1980-2020 with
271 the 200 hPa geopotential height anomalies during the previous period and the same period (a-e). (f-
272 j) and (k-o) Same as in (a-e) but for the 500 hPa and 850 hPa geopotential height anomalies. Dotted
273 blue, solid magenta and solid red lines indicate negative, zero and positive contour values,
274 respectively. All contour intervals are 0.1. The black dotted areas are statistically significant
275 at/above the 90% confidence level.

276

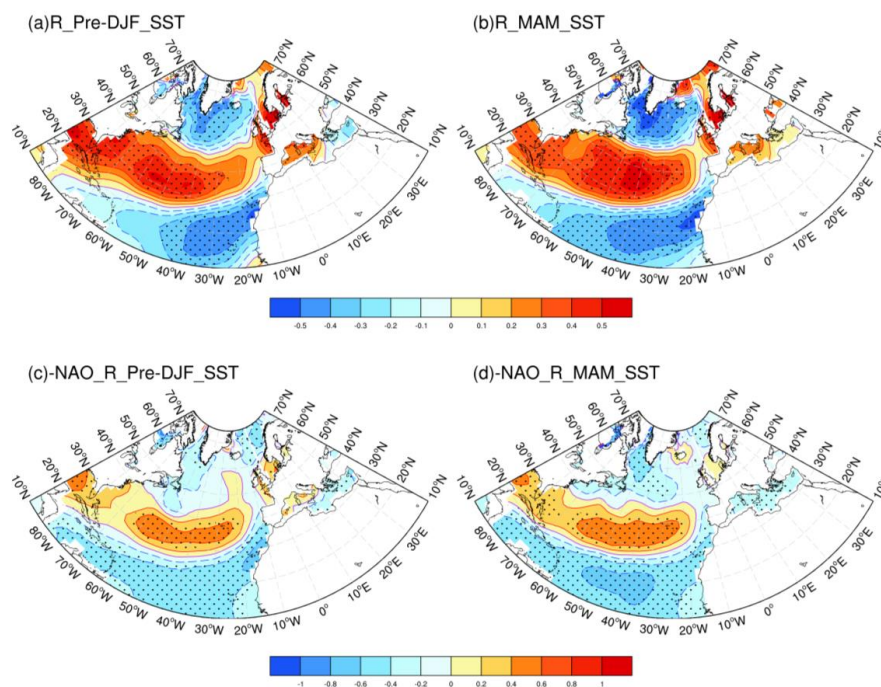


277

278 Figure 3. The monthly standard deviation of the dust column mass density in North China (a) and
279 the NAOI (b) during 1980-2020.

280

281 According to the analysis, the NAOI in boreal winter and late spring DAS in North China have
282 a substantial negative link. How does the boreal winter NAO affect the late spring DAS in North
283 China? There is an obvious correlation between the boreal winter NAOI and both contemporaneous
284 and late North Atlantic SST anomalies (SSTA), as well as a triple-pole model of “-, +, -” (Fig. 4a to
285 b). Previous studies have noted that on seasonal and annual scales, the triple-pole of SST is the
286 primary mode of North Atlantic SST variation, and its variability is closely correlated to the changes
287 in the NAO (Wu et al., 2009). The NAO can modify SST by influencing changes in sea surface wind
288 speed and hence latent heat fluxes in the North Atlantic (Cayan et al., 1992). Simultaneously, the
289 triple-pole SST mode generates atmospheric circulation similar to the NAO, suggesting a positive
290 feedback between them, which has been verified in both observational data analysis (Czaja et al.,
291 2002) and ocean-atmosphere coupled model simulations (Watanabe et al., 2000). These findings
292 show that the SST has a “capacitor effect” on the NAO negative signal, which prolongs the influence
293 of the NAO signal over the surrounding and downstream areas. Moreover, through the correlation
294 distribution between the boreal winter NAOI and both contemporaneous and late North Atlantic
295 SSTA corresponding to the selected NAO negative phase years (1979, 1981, 1984, 1985, 1986, 1995,
296 1997, 2000, 2002, 2003, 2005, 2009, 2010, and 2012), it can be found that the North Atlantic SSTA
297 from boreal winter to late spring is manifested as a “-, +, -” triple-pole pattern characteristic (Fig.
298 4c to d), which further verifies that the early NAO negative signal can be stored in the North Atlantic
299 SST and has an influence on the subsequent weather-climate over the surrounding and downstream
300 regions.



301

302 Figure 4. Correlations of the boreal winter NAOI from 1980-2020 with the SSTA during the
303 previous period and the same period (a-b). (c-d) As in (a-b) but for the NAO negative phase years
304 (1979, 1981, 1984, 1985, 1986, 1995, 1997, 2000, 2002, 2003, 2005, 2009, 2010, and 2012). Dotted
305 blue, solid magenta and solid red lines indicate negative, zero and positive contour values,
306 respectively. And the contour interval is 0.1 (a-b) and 0.2 (c-d), unit: °C. The black dotted areas are
307 statistically significant at/above the 95% confidence level.

308



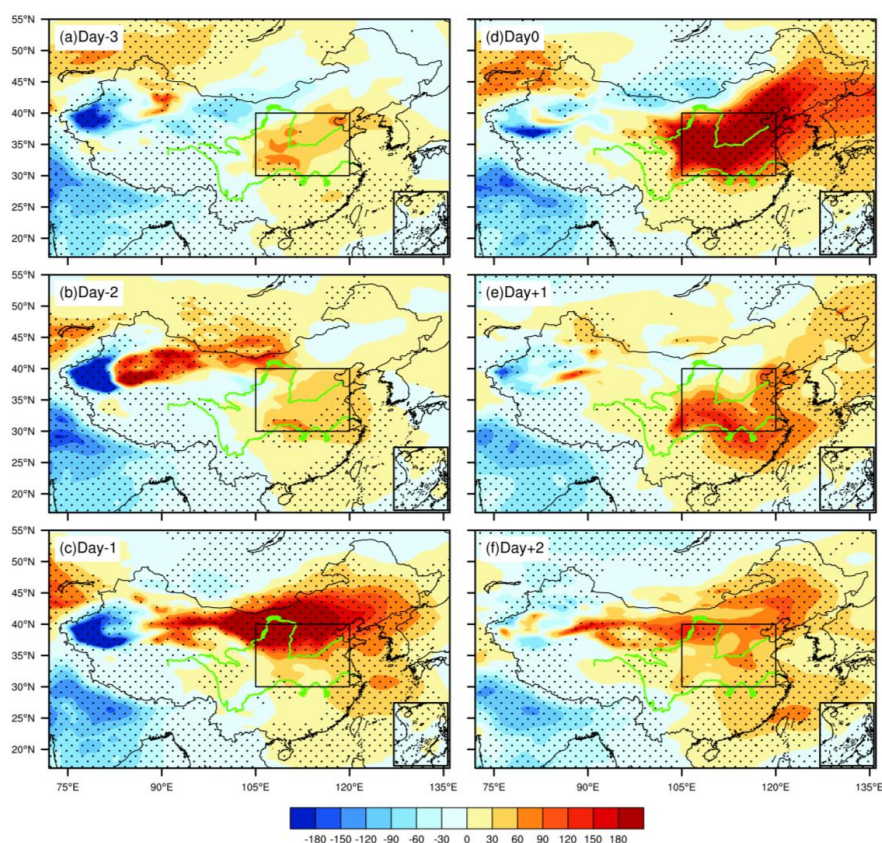
309 **3.2 Atmospheric circulation evolution during DEs**

310 In this paper, we selected 27 spring DEs in North China during the period of 1980-2020 based
311 on the selection criteria, which are distributed over 17 years. It is found that there are shifts of the
312 NAO from a positive to negative phase preceding all the DEs, highlighting the significant influence
313 of the NAO negative phase on the occurrence of DEs. Among these, the 9 DEs (19800419,
314 19820408, 19820502, 19820508, 19850403, 19870317, 19980416, 20100320, 20130309) are
315 striking based on the preliminary unusually strong winter NAO negative signal compared to that
316 before the rest of DEs. At the climate-scale, the NAO intensity in boreal winter of the 9 DEs are all
317 less than -0.5 standard deviations, which corresponds to the NAO negative phase years. Further
318 analysis on the weather-scale indicates that the number of days with NAO negative phase (the value
319 of NAOI less than -0.5) are above 35 days in the 3 months of boreal winter in the 9 DEs. Furthermore,
320 the NAO negative phase is longer and more intense during these 9 DEs, while the NAO negative
321 phase days in the remaining DEs are below 30 days (figure not shown). Therefore, to avoid
322 information filtering caused by too many study cases and to reflect the statistical significance for
323 studying the modulation effect of the NAO negative signal on the DEs in North China to the
324 maximum extent, we chose these 9 DEs with the strongest influence of the NAO negative signal to
325 study the evolution characteristics and synoptic causes of DEs in North China.

326 From the abnormal field of the spatial distribution of DA concentration synthesized by the
327 selected DEs (Fig. 5), it can be found that before the outbreak of DEs, the positive anomalies of DA
328 concentrations appear in the source regions (Xinjiang and Mongolia), and on “Day -1”, the positive
329 anomalous field gradually expands and develops into a positive anomaly belt with maximum values
330 of 180 mg m⁻². At this time, the DA concentrations on the north side of North China already show
331 obvious positive anomalies, providing sufficient source contributions for the outbreak of DEs. On
332 “Day 0”, the overall DA concentration anomaly value exceeds 180 mg m⁻² in North China,
333 indicating that large-scale DEs have broken out. After the outbreak of DEs, the positive DA
334 concentration anomalies in North China decrease rapidly, and the impact of DAs from Xinjiang and
335 Mongolia on North China gradually weakens. Before the outbreak of DEs, the DA concentrations
336 in Mongolia and Xinjiang, which are the primary source areas of DAs in East Asia (Zhang et al.,
337 2003), gradually increase. In the growth process of DA concentrations, DAs are gradually



338 transported eastward to North China. Therefore, the outbreak of DEs in North China is mainly
339 caused by the rapid increase in DA concentrations and their eastward transmission from Xinjiang
340 and Mongolia.
341

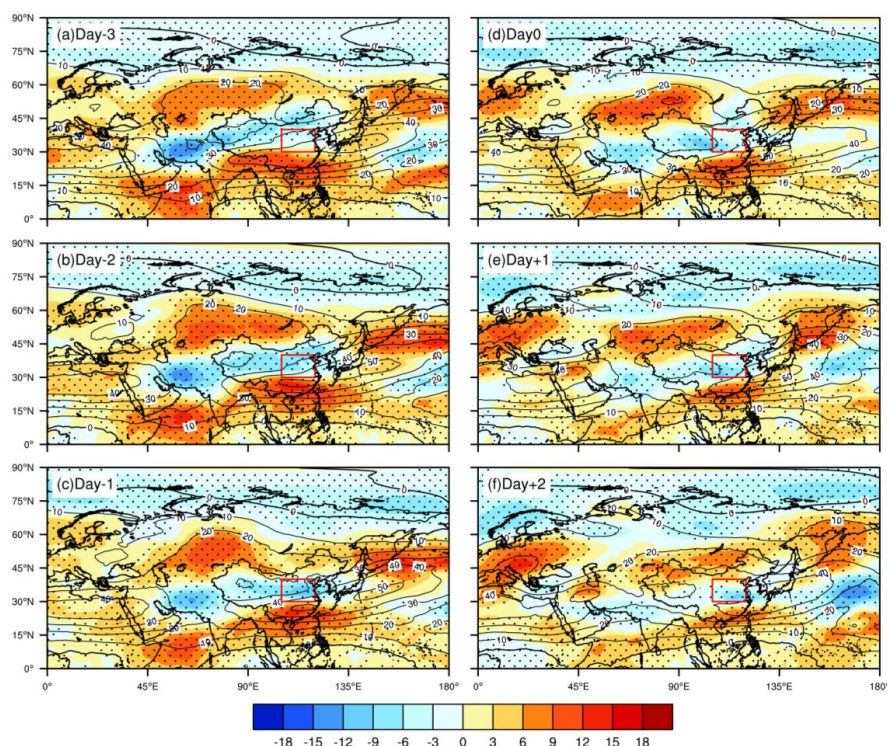


342
343 Figure 5. Spatial distribution of the dust column mass density anomalies in East Asia from “Day -
344 3” to “Day +2” during DEs, unit: mg m^{-2} . The black box indicates the North China study area. The
345 black dotted areas are statistically significant at/above the 95% confidence level.

346
347 The evolution of the 200 hPa atmospheric circulation during DEs is illustrated in Fig. 6,
348 representing features of the wind field in high levels of the troposphere. On “Day -3”, there are
349 large-scale anomalous positive zonal winds in the Siberian area, with positive zonal wind anomalies
350 of $+9 \text{ m s}^{-1}$. From “Day -2” to “Day -1”, the positive zonal wind anomalies move southward,



351 controlling the upstream area of North China (35-50°N, 70-110°E), as well as the desert source areas
352 of Xinjiang and Mongolia. The zonal wind anomalies over the area of North China are in a “+, -, +”
353 triple-pole pattern from the equator to 60°N, indicating that the boreal winter NAO negative signal
354 can propagate to East Asia, resulting in changes in the East Asian subtropical jet stream (EASJS)
355 and polar-front jet stream (PFJS) in late spring. In earlier investigations, similar findings were noted.
356 For example, Shao and Zhang (2012) indicated that when the NAO is unusually strong (weak) in
357 winter, the EASJS will strengthen (weaken) and the PFJS will weaken (strengthen). There are also
358 remarkable features of the EASJS along 30°N, with two centres: the west centre is in northern Africa,
359 with a central intensity of 40 m s⁻¹, and the east centre is situated in the western Pacific south of
360 Japan, with a central intensity of 50 m s⁻¹. As a result of its far distance from the DA source regions
361 in East Asia and North China, the western centre of the EASJS has a very limited impact on these
362 regions. From “Day -3” to “Day -1”, the eastern centre of the EASJS moves eastward, which leads
363 to diminishing zonal winds at 200 hPa in North China, and the negative anomaly centre is lower
364 than -9 m s⁻¹. From “Day 0” to “Day +2”, the eastern centre of the EASJS stops moving eastward
365 and recedes slightly westward, and the zonal winds over North China change to -6 m s⁻¹. Under the
366 effect of vertical circulation, abnormal strong winds at high altitudes can influence middle and low
367 altitude winds through downward momentum transmission, which may lead to the generation of
368 windy weather near the surface (Wu et al., 2016).
369



370

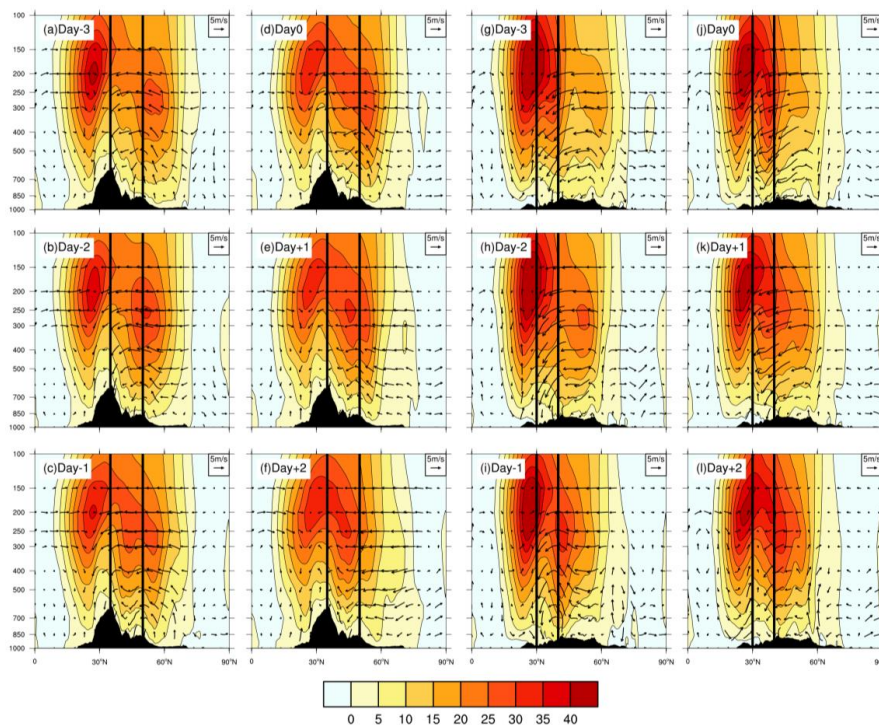
371 Figure 6. Spatial distribution of the 200 hPa winds (contour, unit: m s^{-1}) and their anomalies (shades,
372 unit: m s^{-1}) from “Day -3” to “Day +2” during DEs. The red box indicates the North China study
373 area. The black dotted areas are statistically significant at/above the 95% confidence level.

374

375 To further determine the impact of the upper-level wind speed on the middle-lower wind speed,
376 the vertical pressure-latitude distribution of the mean zonal winds and the vertical winds are
377 calculated over the DA source areas and North China (Fig. 7). As shown in Fig. 7a to f, before the
378 outbreak of DEs, due to the downward momentum of the zonal winds at high altitudes above the
379 DA source areas, the enhancement of the wind speed in the middle-low levels is evident (Wu et al.,
380 2016), resulting in the generation of strong surface wind to meet the dynamic conditions for the
381 uplift of local DAs. After the outbreak of DEs, the average zonal winds in the high levels and the
382 downward momentum effect weaken in DA source areas. Compared with the mean zonal winds in
383 the troposphere over North China (Fig. 7g to i), from “Day -3” to “Day -1”, corresponding to the
384 weakening of the zonal winds in the high levels, the zonal wind speed in the middle-low levels



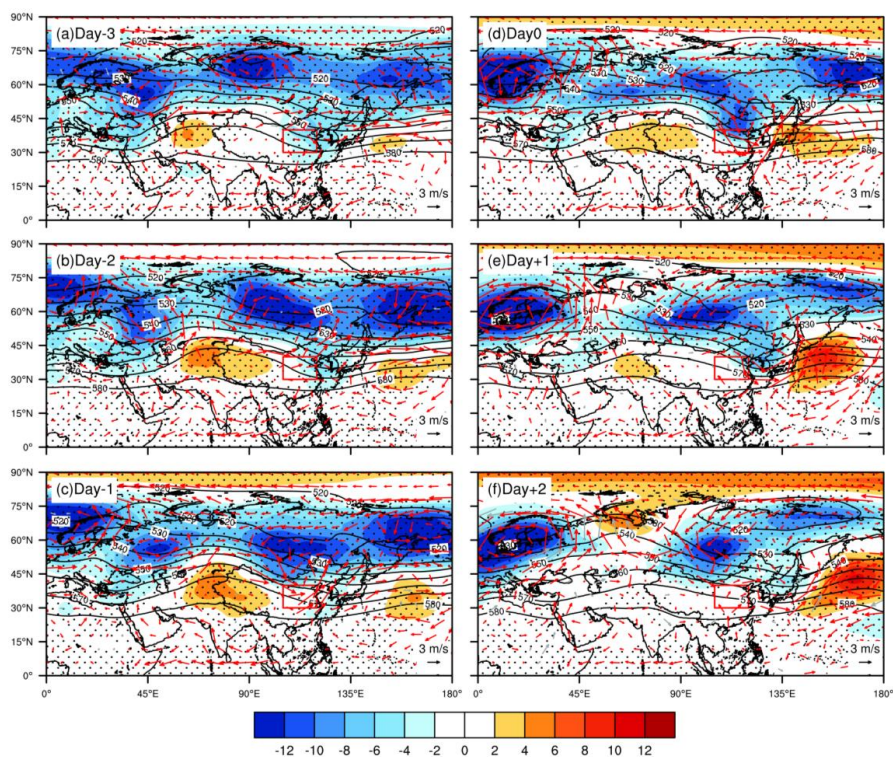
385 decreases due to momentum compensation for the zonal winds in the high levels (Li et al., 2015),
386 which is conducive to the maintenance of DA concentration that is transported before the DE
387 outbreak, as well as in preparation for the subsequent DE outbreak in North China. After the DE
388 outbreak, the zonal winds at high altitudes on the north side of North China strengthen due to the
389 increase in zonal winds in the middle-low levels, and the DA concentration begins to decrease under
390 the effect of strong winds near the surface. It is also noted that during the whole evolution of DEs,
391 the south side of North China is dominated by southerly winds, which have a certain blocking effect
392 on the northward airflow carrying DAs and are favorable for maintaining the DA concentration in
393 North China.
394



395
396 Figure 7. Pressure-latitude cross section of the mean zonal wind [u] (shaded, unit: m s^{-1}) and vertical
397 wind (arrow, (v, w), w expands 100 times, unit: m s^{-1}) averaged over 70° - 110°E from “Day -3” to
398 “Day +2” during DEs. The area surrounded by the black line is the range of the source regions of
399 DA (a-f). (g-l) Same as in (a-f) but for 105° - 120°E . The area surrounded by the black line is the
400 North China study area.



401 In the evolution of atmospheric circulation of DEs at 500 hPa (Fig. 8a to c), the trough-ridge
402 situation is characterized by two troughs and one ridge throughout the high latitudes of the Eurasian
403 continent from “Day -3” to “Day -1”. The two troughs are located in the Black Sea (20-50°E, 30°-
404 60°N) and the eastern part of Russia (105-130°E, 30°-60°N), and the ridge is situated in the Ural
405 Mountains (60-80°E, 25-45°N). The western and eastern troughs both show negative variations
406 before the outbreak of DEs, with maximum values of “-4 dagpm” and “-10 dagpm”, respectively,
407 while the Ural ridge (UR) manifests as gradual enhancement with maximum values of “+6 dagpm”.
408 From “Day 0” to “Day +2”, the intensities of the trough and ridge all gradually weaken (Fig. 8d to
409 f). Before the outbreak of DEs, on account of the strengthening advancement of the trough-ridge
410 situation, the middle-high latitudes are dominated by the strong meridional circulation, the northern
411 cold air transport increases, and the southward invasion of the cold air enhances the local surface
412 wind speed, leading to the uplift of DAs in the DA source areas. After the outbreak of DEs, due to
413 the changes in the trough-ridge situation and the weakening of the UR, the cold air transport
414 weakens, as well as the increasing dust activities and transportation. It should be noted that the UR
415 during DEs is much less than a blocking high based on the intensity as well as the duration. The UR
416 is established on “Day -1” and disappears basically on “Day +1”, which is also consistent with the
417 feature that the maximum duration of DEs does not exceed 2 days (Li et al., 2022).



418

419 Figure 8. The spatial distribution of the 500 hPa geopotential height (contour, unit: dagpm) overlays
420 its anomalies (shades, unit: dagpm) and the 850 hPa wind anomalies (arrows, unit: m s^{-1}) from “Day
421 -3” to “Day +2” during DEs. The red box indicates the North China study area. The black dotted
422 areas and red arrow areas are statistically significant at/above the 95% confidence level.

423

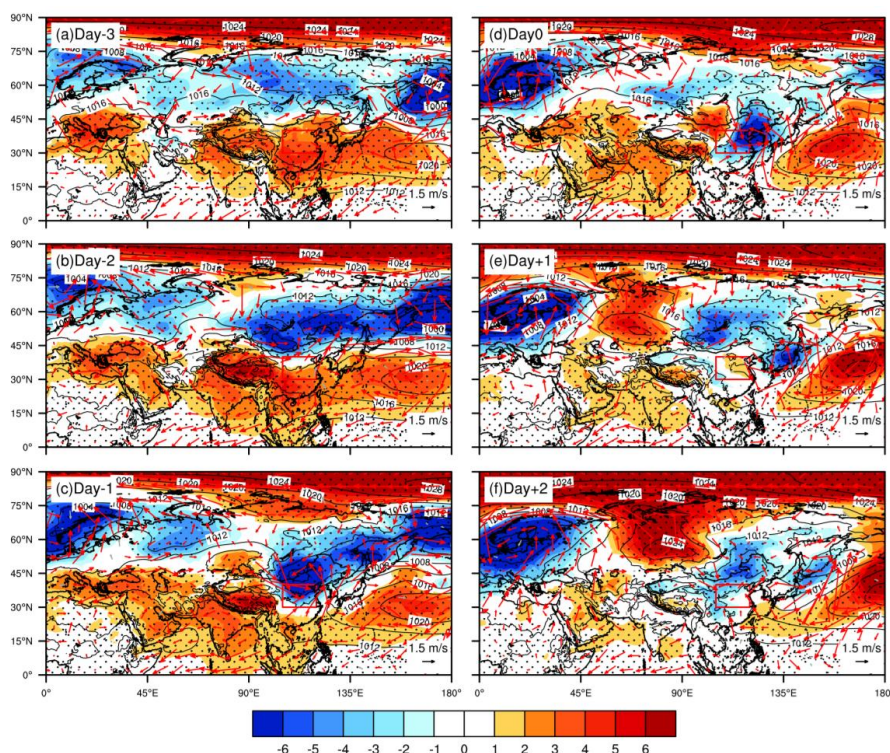
424 There is also a corresponding signal during DEs in the sea level pressure field (Fig. 9). On
425 “Day -3”, North China is controlled by an anticyclonic system dominated by sinking airflow.
426 Therefore, poor precipitation conditions lead to the weak wet-deposition of DAs during transport
427 (Kutieli and Furman, 2003). Meanwhile, the SH starts to appear in the upstream areas of North China.
428 On “Day -2”, the intensity of the SH is enhanced, with maximum values of “+6 hPa”, and moves
429 toward North China, while the intensity of the anticyclonic system controlling North China slightly
430 weakens, and its position does not change significantly. In Mongolia, the MC starts to develop,
431 accompanied by strong winds and vertical upward flows induced by the MC, which is conducive to
432 the dynamic circumstances for the development uplift of DAs. On “Day -1”, the location and



433 intensity of the SH both change little, while the intensity of the anticyclonic system controlling
434 North China weakens and even tends to disappear, and the intensity of the MC increases and moves
435 slightly southward. On “Day 0”, the SH moves eastward to the territory of Mongolia, and the MC
436 moves southeastward, which is conducive to the transport of DAs from Mongolia to North China.
437 From “Day +1” to “Day +2”, the intensities of both the SH and MC start to weaken, and the impact
438 on North China begins to weaken. In summary, under the negative phase of the NAO, before the
439 outbreak of DEs, due to the establishment, strengthening and southward movement of the SH and
440 MC, there is a wide range of northerly winds and the outbreak of cold air to the south, which is
441 advantageous for the uplift and transmission of DAs to North China. Simultaneously, North
442 China is controlled by an anticyclonic system, leading to local weather, mainly sunny conditions
443 and weak winds, which is also favorable for the transport of DAs to North China. After the
444 outbreak of DEs, both the SH and MC start to weaken, indicating that the uplift of DAs in the
445 DA source areas and the dust transmission activities to North China start to weaken.

446 From the above atmospheric circulation characteristics, under the NAO negative phase, the
447 crucial synoptic systems leading to DE occurrences in North China are the abnormal winds by the
448 anomalies of the upper-level EASJS, the UR, the SH and the frontal cyclone (MC) near the surface.
449 In addition, transient eddy is crucial for the abnormal evolution of atmospheric circulation. The
450 mechanisms of the formation of these synoptic system anomalies from the view of transient eddy
451 are investigated to reveal the mechanism of the synoptic cause for the DEs in North China under
452 the modulation of the NAO negative phase.

453



454

455 Figure 9. Spatial distribution of the sea level pressure (contour, unit: hPa) overlays with its
456 anomalies (shades, unit: hPa) and the 1000 hPa wind anomalies (arrows, unit: m s^{-1}) from “Day -3”
457 to “Day +2” during DEs. The red box indicates the North China study area. The black dotted areas
458 and red arrow areas are statistically significant at/above the 95% confidence level.

459

460 3.3 Transient eddy flux transport characteristics during DEs

461 Transient eddy fluctuations contribute to the maintenance of the atmospheric energy balance
462 through energy transport, and the energy transport process causes the divergence and convergence
463 of energy and mass between different regions, thus forming new regions of forcing within the
464 atmosphere (Li et al., 2019b). Transient eddy flux transport can enhance the positive pressure
465 component of the mean airflow and compensate for ground friction, which has a significant effect
466 on the maintenance of atmospheric circulation. For example, transient eddy momentum transport is
467 associated with the development of blocking high generation, and momentum transport contributes
468 differently during each period of its development (Li et al., 2019b). DE occurrences are inevitably

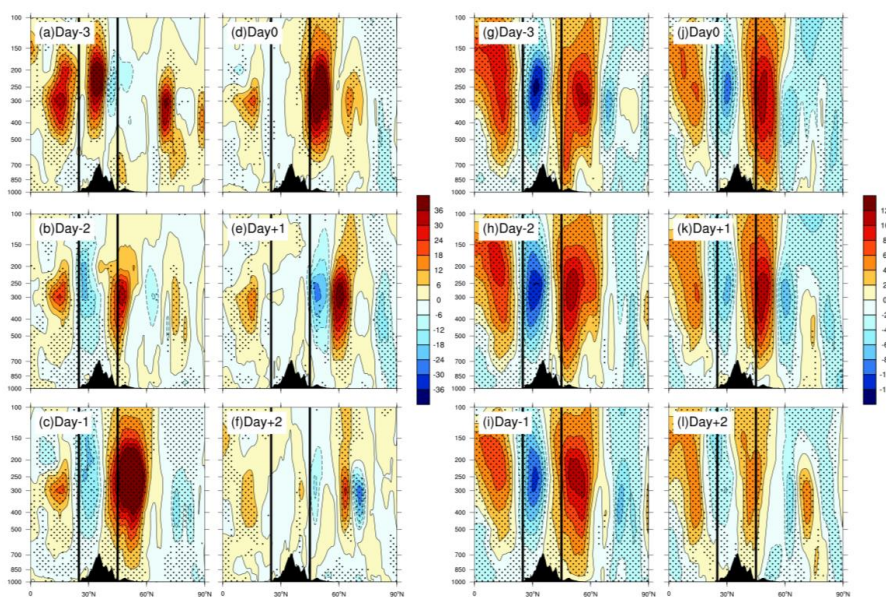


469 accompanied by tropospheric atmospheric circulation anomalies, and transient eddy flux transport
470 plays a significant role in the process of atmospheric circulation. Therefore, the possible
471 mechanisms of transient eddy momentum and heat transport during DEs under the NAO negative
472 phase on the change in major synoptic system anomalies are further analysed and explored.

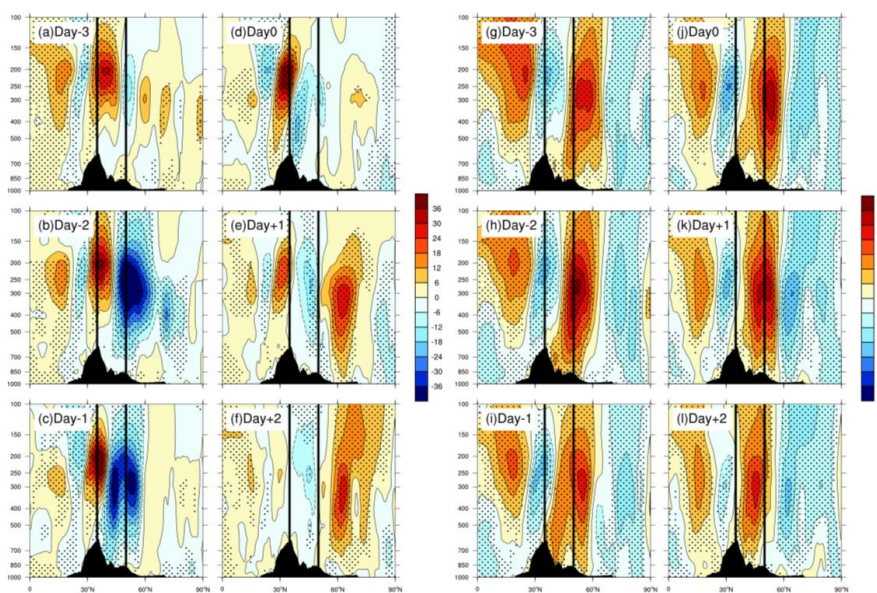
473 The “+” (“-”) sign of $[u'v']$ implies the poleward (equatorward) transport of transient eddy
474 momentum, and the “+” (“-”) sign of $[u']$ represents the positive (negative) anomaly of the zonal
475 winds. Analysing the transport features of transient eddy momentum within the active range of the
476 UR during DEs (Fig. 10a to f), it is found that a pattern of “positive south and negative north”
477 appears with poleward, equatorward momentum transport near 30°N and 40°N at approximately
478 200-500 hPa on “Day -3”, respectively, while a $[u'v']$ convergence centre exists within the area of
479 the UR. On “Day -2”, the feature of $[u'v']$ in the Urals region changes from convergence to
480 divergence, and on “Day-1”, the “negative south and positive north” pattern of transient eddy
481 momentum reaches the highest value during DEs, with maximum values of $-24\text{ m}^2\text{ s}^{-2}$ and $+30\text{ m}^2$
482 s^{-2} , respectively. After the outbreak of DEs, the intensity of the $[u'v']$ centre in the Urals region
483 rapidly decreases, with no longer obvious $[u'v']$ transport. For the zonal wind anomalies $[u']$ (Fig.
484 10g to l), before the outbreak of DEs, $[u']$ in the Urals region there is a “negative south and positive
485 north” mode, which is mainly controlled by negative $[u']$, with maximum values of -12 m s^{-1} ,
486 corresponding to divergence of $[u'v']$. From “Day 0” to “Day +1”, the UR region gradually becomes
487 dominated by the “+” signal of $[u']$. On “Day +2”, as there is unobvious $[u'v']$ within the region of
488 the UR, the intensity of $[u']$ weakens rapidly. Investigation of the transient eddy momentum
489 transport characteristics and the changes in the zonal wind anomalies during DEs show that there is
490 an obvious divergence centre of the transient eddy momentum within the range of UR before the
491 outbreak of DEs, corresponding to zonal wind weakening and the establishment of meridional
492 circulation. Therefore, transient eddy momentum transport has an indirect influence on the
493 establishment and advancement of the UR (Li et al., 2022). To obtain a better understanding of the
494 role of transient eddy momentum on anomalies of the wind field during DEs, the $[u'v']$
495 characteristics of the DA source areas are further analysed (Fig. 11a to f). The transient eddy
496 momentum pattern of “positive south and negative north” in the DA source areas is gradually
497 displayed at 200-500 hPa from “Day -3” to “Day -1”, with maximum values of $+36\text{ m}^2\text{ s}^{-2}$ and -36



498 $\text{m}^2 \text{s}^{-2}$, respectively. After the outbreak of DEs, the source areas of DAs are mainly controlled by the
499 weak $[u'v']$ negative centre, with unobvious transient eddy momentum. For the zonal wind
500 anomalies $[u']$ (Fig. 11g to l), before the outbreak of DEs, the DA source regions gradually become
501 dominated by positive $[u']$, with maximum values of $+10 \text{ m s}^{-1}$ on account of the convergence of
502 transient eddy momentum, facilitating the uplift of DAs. After the outbreak of DEs, $[u']$ still
503 predominantly increases, indicating that there are more complex reasons for the zonal wind changes
504 than the transport of transient eddy momentum, which deserves in-depth analysis later.
505



506
507 Figure 10. Pressure-latitude cross section of the mean transient momentum $[u'v']$ (unit: $\text{m}^2 \text{s}^{-2}$) (a-f)
508 and the zonal wind anomalies $[u']$ (unit: m s^{-1}) (g-l) averaged over $60^\circ\text{-}80^\circ\text{E}$ from “Day -3” to “Day
509 +2” during DEs. The area surrounded by the black line is the range of the UR. The black dotted
510 areas are statistically significant at/above the 95% confidence level.



511

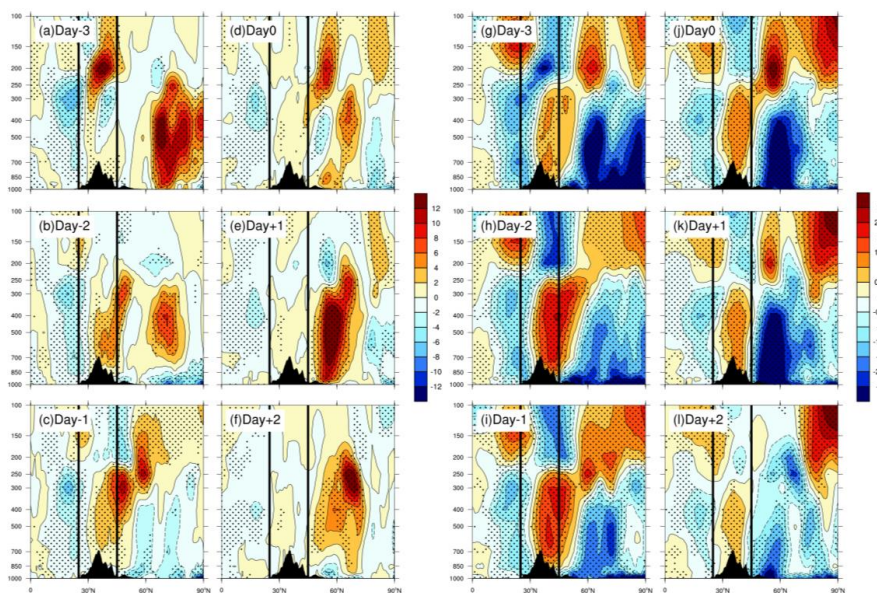
512 Figure 11. Pressure-latitude cross section of the mean transient momentum $[u'v']$ (unit: $\text{m}^2 \text{s}^{-2}$) (a-f)
513 and the zonal wind anomalies $[u']$ (unit: m s^{-1}) (g-l) averaged over $70^\circ\text{--}110^\circ\text{E}$ from “Day -3” to “Day
514 +2” during DEs. The area surrounded by the black line is the range of the source regions of DA.
515 The black dotted areas are statistically significant at/above the 95% confidence level.

516

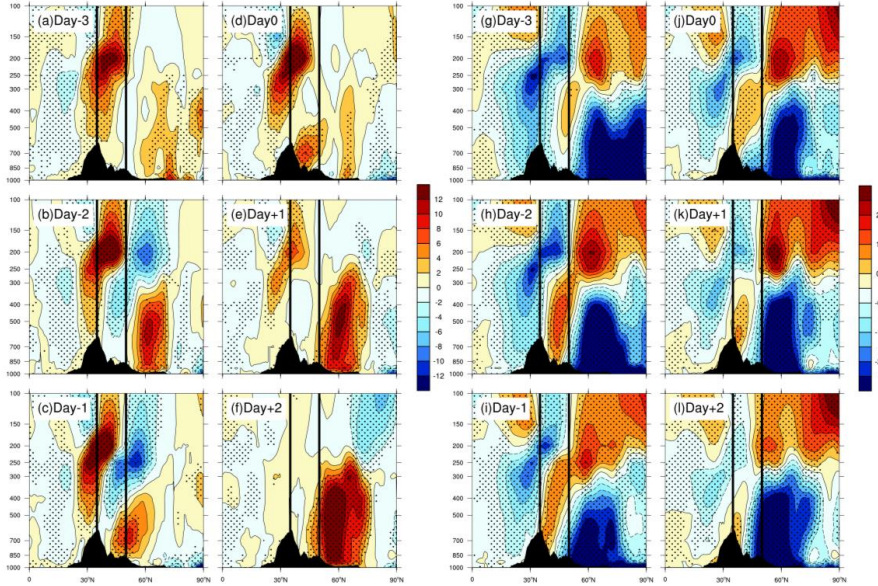
517 Atmospheric circulation also heavily depends on transient eddy heat transport (Li et al., 2019b;
518 Li et al., 2022). Similar to the features of transient eddy momentum transport, the “+” (“-”) sign of
519 $[v'T']$ describes the poleward (equatorward) transport of transient eddy heat, and the “+” (“-”) sign
520 of $[T']$ implies an increase (decrease) in temperature. In the analysis of the $[v'T']$ characteristics
521 within the range of UR during DEs (Fig. 12a to f), it is found that the convergence of transient eddy
522 heat is dominant at 200-500 hPa on “Day -3”, with maximum values of $+12 \text{ m s}^{-1} \text{ K}$ and $-6 \text{ m s}^{-1} \text{ K}$,
523 respectively. During the subsequent “Day -2” to “Day -1”, the UR area is dominated by a strong
524 positive $[v'T']$ centre, which also exhibits the convergence features of transient eddy heat. There are
525 unobvious features of $[v'T']$ in the developmental range of the UR from “Day 0” to “Day +2”. In the
526 analysis of the temperature anomalies $[T']$ (Fig. 12g to l), it is shown that before the outbreak of
527 DEs, the area with developed UR is in the convergence region of transient eddy heat, and $[T']$
528 becomes more visible when the transient eddy heat transport increases, showing a “negative south



529 and positive north” pattern below 300 hPa. The temperature gradient ($-\partial T / \partial y$) is weakened here
530 by the thermal wind formula ($u_T = -R \cdot \partial T / \partial y$, where u_T , R , and T demonstrate the thermal
531 wind, gas constant and temperature, respectively), and the thermal wind will be weakened due to
532 the decline in the temperature gradient. When the thermal wind is weakened, the zonal winds are
533 also weakened, which facilitates the establishment of meridional circulation and the development
534 of a blocking situation (Li et al., 2019b). After the outbreak of DEs, $[T']$ decreases due to the
535 weakening of the transient eddy heat transport. From “Day 0” to “Day +1”, the negative $[T']$
536 anomaly centre appears north of the UR, and the negative $[T']$ centre gradually moves southward,
537 which corresponds to the increase in the temperature gradient here and is not favorable to the
538 development of the UR. The transient eddy heat transport also has an impact on the wind field for
539 the source regions of DAs (Fig. 13a to c). Before the outbreak of DEs, the $[v'T']$ over the DA source
540 areas gradually evolves to be dominated by the convergence above 300 hPa, while the divergence
541 of $[v'T']$ is dominated below 300 hPa. The strongest $[v'T']$ convergence and divergence
542 characteristics are both reached on “Day -1”. After the outbreak of DEs (Fig. 13d to f), the DA
543 source regions are controlled by a positive $[v'T']$ centre, with the convergence of $[v'T']$ on “Day 0”.
544 From “Day +1” to “Day +2”, there are unobvious $[v'T']$ features over the source areas of DAs.
545 Analysis of the temperature anomalies $[T']$ (Fig. 13g to l) reveals that below 300 hPa in the DA
546 source regions before the outbreak of DEs, the transient eddy heat transport weakens with time due
547 to the “positive south and negative north” mode of $[T']$, with maximum values of +2 K and -2 K,
548 respectively. The temperature gradient is enhanced, and the development of thermal wind leads to
549 the enhancement of zonal winds. In addition, the zonal winds in the middle-low levels are enhanced
550 by the enhanced thermal wind, and the momentum downward transport of zonal winds in the high
551 levels further enhances the zonal winds in the middle-low levels, which is conducive to the uplift of
552 DAs. In addition, the convergence of $[v'T']$ is unfavorable to the development of the zonal winds
553 above 300 hPa according to the thermal wind formula, which hinders the momentum downward
554 transport of the zonal winds in the high levels in the DA source areas. Transient momentum transport
555 has a greater effect on the variability of zonal winds at high levels than transient eddy heat transport
556 (Solomon, 1997).
557



558
559 Figure 12. Pressure-latitude cross section of the mean transient heat [$v'T'$] (unit: $\text{m s}^{-1} \text{K}$) (a-f) and
560 temperature anomalies [T'] (unit: K) (g-l) averaged over $60^\circ\text{-}80^\circ\text{E}$ from “Day -3” to “Day+2” during
561 DEs. The area surrounded by the black line is the range of the UR. The black dotted areas are
562 statistically significant at/above the 95% confidence level.
563



564

565 Figure 13. Pressure-latitude cross section of the mean transient heat [$v'T'$] (unit: $\text{m s}^{-1} \text{K}$) (a-f) and
 566 temperature anomalies [T'] (unit: K) (g-l) averaged over $70^\circ\text{-}110^\circ\text{E}$ from “Day -3” to “Day +2”
 567 during DEs. The area surrounded by the black line is the range of the source regions of DA. The
 568 black dotted areas are statistically significant at/above the 95% confidence level.

569

570 The transient eddy flux transport characteristics during DEs show that the changes in [$u'v'$] and
 571 [$v'T'$] in the DA source regions and the active range of the UR cause both energy and mass
 572 divergence in North China, leading to diminishing zonal winds at high levels over North China
 573 during DEs. Meanwhile, the zonal winds in the middle-low levels weaken through vertical
 574 circulation, accompanied by southerly airflow on the south side of North China, facilitating DA
 575 concentration.

576 Results of the previous analysis of the transient eddy flux transport characteristics indicate that
 577 the evolution of the UR may be explained by the divergence of transient eddy momentum and the
 578 convergence of transient eddy heat by the thermal wind formula. By using the equation for the quasi-
 579 geostrophic potential, this mechanism can also be verified (Gary, 2011) as follows:

580

$$\left[\nabla^2 + \frac{\partial}{\partial p} \cdot \left(\frac{f^2}{\sigma} \cdot \frac{\partial}{\partial p} \right) \right] \cdot \frac{\partial \Phi}{\partial t} = -f \cdot \bar{V}_g \cdot \nabla (\xi_g + f) - \frac{\partial}{\partial p} \cdot \left[-\frac{f^2}{\sigma} \cdot \bar{V}_g \cdot \nabla \left(-\frac{\partial \Phi}{\partial p} \right) \right] \quad (3)$$



581 where f , Φ , and \overline{V}_g denote the Coriolis parameter, geopotential height, and geopotential wind,
 582 respectively, and $\sigma = -\frac{RT}{p} \cdot \frac{\partial \ln \theta}{\partial p}$, $\xi_g = \frac{\partial v_g}{\partial x} - \frac{\partial u_g}{\partial y} = \frac{1}{f} \cdot \nabla^2 \Phi$ denote the static stability and
 583 the geostrophic relative vorticity, respectively. The first and second terms on the right-hand side of
 584 the equal sign of Eq. (3) have the following equivalence after simplification:

$$585 \quad -\frac{\partial \Phi}{\partial t} \propto -\overline{V}_g \cdot \nabla \xi_g \quad (4)$$

$$586 \quad -\frac{\partial \Phi}{\partial t} \propto \frac{\partial}{\partial p} (-\overline{V}_g \cdot \nabla T) \quad (5)$$

587 On the trough-ridge lines, since the vorticity advection in Eq. (4) is zero and the height of the
 588 isobaric surface has no change, it only moves the ridges and does not change the strength of the
 589 ridges. The temperature advection in Eq. (5) mainly acts on the trough-ridge lines, which affects the
 590 development of the trough-ridge intensity but has no influence on its movement. In this study, we
 591 mainly consider the change in trough-ridge intensity during DEs by noting the effect of temperature
 592 advection. Temperature advection generally decreases with height, so it is sufficient to discuss only
 593 the signs of positive and negative temperature advection here. Analysis of transient eddy heat
 594 transport characteristics reveal that the transport of transient eddy heat in the UR region before the
 595 outbreak of DEs will lead to uneven temperature distribution, which in turn leads to the development
 596 of warm advection. The analysis of the quasi-geostrophic potential theory shows that the
 597 development of warm advection in this region is beneficial to the development of the UR and to the
 598 establishment of a temperature ridge. After the outbreak of DEs, the temperature advection starts to
 599 weaken as $[\nu T]$ no longer change within the area of UR, and thus, the intensity of UR also starts to
 600 weaken.

601 Meanwhile, the active development of temperature advection and vorticity advection due to
 602 transient eddy heat transport and the enhancement of UR, based on the Ω equation in the quasi-
 603 geostrophic theory (Gary, 2011), can also explain abnormal evolutions of the SH as well as the MC
 604 near the surface during DEs, as follows:

$$605 \quad \left(\nabla^2 + \frac{f^2}{\sigma} \cdot \frac{\partial^2}{\partial p^2} \right) \omega = \frac{f}{\sigma} \cdot \frac{\partial}{\partial p} \left[\overline{V}_g \cdot \nabla (\xi_g + f) \right] + \frac{1}{\sigma} \cdot \nabla^2 \left[\overline{V}_g \cdot \nabla \left(-\frac{\partial \Phi}{\partial p} \right) \right] \quad (6)$$

606 where f , ω , \overline{V}_g , and Φ denote the Coriolis parameter, vertical velocity, geopotential height,



607 and geopotential wind, respectively, and $\sigma = -\frac{RT}{p} \cdot \frac{\partial \ln \theta}{\partial p}$, $\omega = \frac{dp}{dt}$, and $\xi_g = \frac{\partial v_g}{\partial x} - \frac{\partial u_g}{\partial y} = \frac{1}{f} \cdot \nabla^2 \Phi$
608 denote the static stability, vertical velocity, and geostrophic relative vorticity, respectively. After
609 simplification, the first and second terms in Eq. (6) to the right of the equal sign are equivalent to
610 the following:

$$611 \quad \omega \propto \frac{\partial}{\partial p} \cdot \left[-\vec{V}_g \cdot \nabla \xi_g \right] \quad (7)$$

$$612 \quad \omega \propto \vec{V}_g \cdot \nabla T \quad (8)$$

613 According to Eq. (7) and (8), the relationship between the vertical velocity and vorticity
614 advection and temperature advection can be obtained, respectively. When the positive (negative)
615 vorticity advection increases with height, the degree of counterclockwise (clockwise) rotation
616 increases there, and the divergence (convergence) increases with height under the Coriolis force,
617 which will produce the rising (sinking) motion. As the vorticity advection generally increases with
618 height, it is sufficient to discuss only the signs of positive and negative vorticity advection here. In
619 short, it is expressed as warm (cold) advection corresponding to the rising (sinking) motion. Before
620 the outbreak of DEs, the northwest winds in front of the UR are strengthened along with the
621 enhancement of the ridge, and the northwest winds correspond to the development of negative
622 vorticity advection and cold advection. According to the quasi-geostrophic theory, a sinking motion
623 will be generated in front of the UR, which corresponds to pressurization at the surface and will
624 promote the establishment, strengthening, and southward movement of the SH. Similarly, the
625 Mongolian region is located in front of the trough at this time, controlled by the southwesterly winds.
626 Corresponding to the development of positive vorticity advection and warm advection here, an
627 upward motion will be generated in Mongolia, corresponding to depressurization at the surface,
628 which will promote the establishment, enhancement, and southward movement of MC there.
629 After the outbreak of DEs, both the SH and MC start to weaken by reversal impacts of the
630 temperature and vorticity advectations due to the weakening of the trough-ridge situation at a deeper
631 level due to the change in transient eddy transport conditions.

632

633 **4 Conclusions and discussions**

634 As a significant extra-equatorial mode of low-frequency atmospheric variability with a periodic



635 signal on the seasonal-scale in the NH and a dominant mode of seasonal to annual winter semi-
636 annual variability, the NAO has an influence on the DEs in East Asia, with significant regional
637 characteristics. The spring DA concentration in North China, a non-dust source region, exhibits high
638 values and strong annual variability. In this study, it is found that the boreal winter NAO negative
639 signal has a significant effect on the DEs in late spring in North China. Modulated by the NAO
640 negative signal, the tropospheric weather situation shows obvious anomalies, and the evolution
641 mechanism can be revealed from the perspective of transient eddy transport.

642 The boreal winter NAO negative signal through the “capacitor effect” of the North Atlantic
643 prolongs its atmospheric signal and influences the late spring DEs in North China. Under the
644 modulation impact of the upstream NAO negative signal, the zonal winds at 200 hPa above the DA
645 source regions gradually increase before the outbreak of DEs, and the increased zonal winds in the
646 high levels transport the momentum to the zonal winds in the middle-low levels through the vertical
647 circulation, which is favorable to the uplift of DAs in the DA source areas. Meanwhile, the zonal
648 wind in the high levels is dominated by negative anomalies over North China, which has a counter
649 effect on the zonal winds in the middle-low levels by vertical circulation and facilitates the
650 maintenance of DA concentrations in North China. At 500 hPa, meridional circulation is obvious in
651 Eurasia continent, and the UR is established, which is favorable for the accumulation of upper-level
652 cold air and the activities of lower-level cold air. Near the surface, the SH and MC are established,
653 enhanced and move southward, providing the northerly airflow in front of the DA source regions,
654 guiding the cold air at high latitudes southward and acting favourably to the uplift and transmission
655 of DAs to downstream North China. Simultaneously, the south side of North China is dominated by
656 southerly winds, which have a blocking effect on the northerly airflow carrying DAs, facilitating
657 the maintenance of DA concentrations in North China. After the outbreak of DEs, both favorable
658 atmospheric circulations weaken gradually, and the DAs also start to decrease in North China.

659 Transient eddy has an important effect on the synoptic evolution of DEs through the
660 modulation of the NAO negative signal. In advance of the outbreak of DEs, the transient eddy
661 momentum at 300-500 hPa above the DA source region is dominated by convergence, and thus, the
662 zonal winds are enhanced. Meanwhile, the characteristics of transient eddy heat over the source
663 areas of DAs are mainly divergence, and the temperature anomalies are in a “positive south and

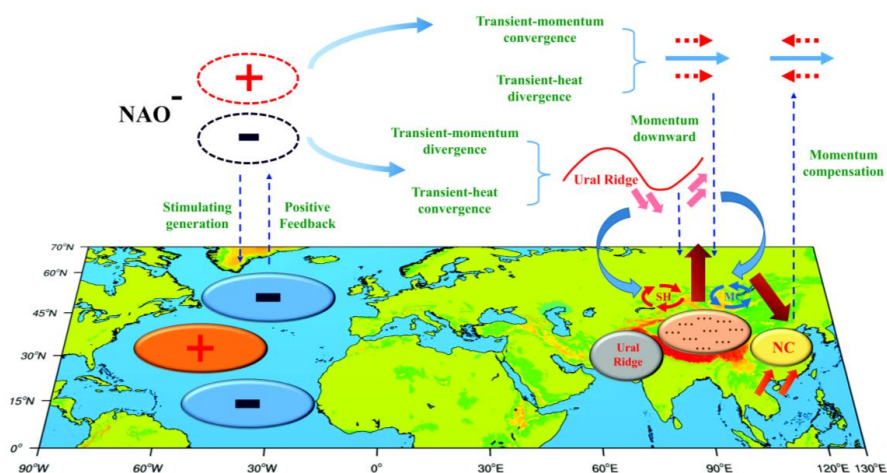


664 negative north” pattern, resulting in enhancement of the temperature gradient and the zonal winds.
665 Therefore, the zonal winds over the DA source regions increased by both the downward momentum
666 and thermal wind, which is favorable to the uplift of DAs. Within the area of UR, the transient eddy
667 momentum (heat) diverges (converges). The divergence of transient eddy momentum will lead to
668 the weakening of zonal winds, while the decrease in zonal winds and the reduction in temperature
669 gradients are both favoured by the convergence of transient eddy heat. The establishment and growth
670 of the meridional circulation are significantly influenced by both, which is conducive to the
671 development of the UR. The changes in upstream transient eddy flux transport cause both energy
672 and mass divergence in North China, resulting in diminishing zonal winds during DEs. After the
673 outbreak of DEs, the transient eddy flux transport characteristics in both the Ural region and the
674 source areas of DAs gradually weaken, and the effect on the zonal winds within these regions is also
675 reduced.

676 In this study, we examine how the late spring DEs in North China are impacted by the boreal
677 winter NAO negative signal and the corresponding synoptic mechanism from the view of transient
678 eddy flux transport on the weather-scale by selecting 9 DEs from 1980 to 2020. Our focus is
679 different from previous analyses of the NAO and the DEs in China on the seasonal climate-scale
680 (Tang et al., 2005; Zhao et al., 2012). The findings demonstrate that the boreal winter NAO negative
681 signal can store its signal in the North Atlantic as a triple-pole structure of “-, +, -”, which then
682 releases in late spring and affects the anomaly of atmospheric circulation in the troposphere by
683 transient eddy flux transport, as well as the zonal winds over the DA source regions and North China.
684 The thermal wind principle and the quasi-geostrophic theory can both explain this mechanism.
685 According to changes in the temperature gradient, the thermal wind principle directly explains
686 variations in the wind fields by the convergence and divergence of the thermal and momentum
687 transient eddy flux during DEs. The quasi-geostrophic theory can illustrate the abnormal formation
688 mechanism of synoptic systems in the whole troposphere during DEs. To be more precise, the
689 influence of the NAO negative signal in transient eddy fluxes causes temperature and vorticity
690 advection to develop; therefore, both mid-upper-level systems (the UR) and surface systems (the
691 SH and MC) strengthen, which can be explained by the height tendency equation and Ω equation,
692 respectively. The development of the above synoptic systems is favorable to the uplift of DAs
693 in the DA source areas and the transmission process to North China. Meanwhile, the southward



694 airflow on the south side of North China is favorable for maintaining the stable high value of DA
695 concentration for 1-2 days. The results are illustrated in Fig. 14, which displays the main synoptic
696 systems and transient eddy flux transport characteristics during DEs against the background of the
697 NAO negative phase. The result is helpful for a thorough comprehension of the mechanism
698 underlying the formation of DEs in eastern China and could serve as a point of reference for the
699 seasonal forecasting of DEs (Shao et al., 2003; Hong et al., 2019).
700



701
702 Figure 14. A schematic diagram of the main synoptic system anomalies and the role of transient
703 eddy fluxes during DEs.
704

705 In addition to transient eddy, stationary eddy is also crucial in the development of atmospheric
706 circulation, and the energy transport of stationary eddy differs from that of transient eddy, and has
707 been applied to the analysis of atmospheric circulation processes such as the UR (Li et al., 2019c).
708 To further advance our knowledge of dust hazards at the regional-scale in China, the impacts of
709 various forms of energy transport on the synoptic systems of DEs in China will be concurrently
710 considered in future work. Globally, the majority of DAs are found in arid and semi-arid areas, and
711 the most widespread and longest-lasting source regions of DAs are located in the NH, forming a
712 dust belt starting from the west coast of northern Africa and extending through the Arabian
713 Peninsula and central and southern Asia to eastern China (Washington et al., 2003; Ginoux et al.,
714 2012). In this study, the contribution of DA source regions in East Asia to the DEs in North China



715 is mainly considered, but insufficient consideration is given to other DA source regions. In further
716 studies, more study methods, such as numerical simulations, should be applied to fully explore the
717 role of DA transport from the NH source areas of DAs to China and to elucidate the details of the
718 development of DEs in China. In addition, the DEs in China are also impacted by other factors that
719 are related to the NAO, such as the ENSO (Li et al., 2021b; Yang et al., 2022). Previous research
720 has demonstrated that central Pacific El Niño events can stimulate the negative phase of the NAO
721 by transmitting the Pacific signal to the north Atlantic through a “subtropical bridge” mechanism,
722 while this association is insignificant for eastern Pacific El Niño events (Graf and Zanchettin, 2012).
723 Zhang et al. (2015) also discovered that the north Atlantic jet stream strengthens and the NAO
724 exhibits a positive phase during central Pacific La Niña events, whereas the north Atlantic jet stream
725 weakens and the NAO exhibits a negative phase during eastern Pacific La Niña events. In the
726 context of global warming, the SSTA of the tropical Pacific mainly exhibits a cold tongue mode,
727 and the positive phase of the cold tongue mode can easily stimulate central Pacific El Niño events
728 (Li et al., 2017). However, it is not clear how the connection between the NAO and ENSO will
729 evolve under global warming. Therefore, it is worthwhile to continue researching the synergistic
730 effect of the NAO and ENSO on the DEs in China.

731

732 **Code and data availability.** The MERRA-2 dust aerosol concentrations dataset can be downloaded
733 from <https://disc.gsfc.nasa.gov/datasets?project=MERRA-2> (last access: 12 January 2023). The
734 atmospheric reanalysis datasets, including the wind field, geopotential height field, sea level
735 pressure field, temperature field, and vertical velocity field can be downloaded from
736 <https://cds.climate.copernicus.eu/#/search?text=ERA5&type=dataset> (last access: 12 January
737 2023). Our results can be made available upon request.

738

739 **Author contributions.** YL, FLX, and JF conceptualized and designed the research. FLX
740 synthesized and analyzed the data. YL, FLX, and JF produced the figures. CL and WJZ contributed
741 to the MERRA-2 dataset retrieval. All the authors including MYD, WJS discussed the results and
742 wrote the paper.

743



744 **Competing interests.** The authors declare that they have no conflict of interest.

745

746 **Disclaimer.** Publisher's note: Copernicus Publications remains neutral with regard to jurisdictional
747 claims in published maps and institutional affiliations.

748

749 **Acknowledgements.** This research has been supported by the National Key Research &
750 Development (R&D) Program of China (Grant/Award Number: 2019YFA0606801).

751

752 **Financial support.** This research has been supported by the National Key Research & Development
753 (R&D) Program of China (Grant/Award Number: 2019YFA0606801).

754

755 **References**

756 Ackerman, A. S., Toon, O. B., Stevens, D. E., Heymsfield, A. J., Ramanathan, V., and Welton, E. J.:
757 Reduction of tropical cloudiness by soot, *Science*, 288, 1042-1047,
758 <https://doi.org/10.1126/science.288.5468.1042>, 2000.

759 An, L. C., Che, H. Z., Xue, M., Zhang, T. H., Wang, H., Wang, Y. Q., Zhou, C. H., Zhao, H. J., Gui,
760 K., Zheng, Y., Sun, T. Z., Liang, Y. X., Sun, E. W., Zhang, H. D., and Zhang, X. Y.: Temporal and
761 spatial variations in sand and dust storm events in East Asia from 2007 to 2016: Relationships
762 with surface conditions and climate change, *Sci. Total Environ.*, 633, 452-462,
763 <https://doi.org/10.1016/j.scitotenv.2018.03.068>, 2018.

764 Cayan, D. R.: Latent and Sensible Heat Flux Anomalies over the Northern Oceans: The Connection
765 to Monthly Atmospheric Circulation, *J. Clim.*, 5, 354-369, [https://doi.org/10.1175/1520-0442\(1992\)005<0354:Lashfa>2.0.Co;2](https://doi.org/10.1175/1520-0442(1992)005<0354:Lashfa>2.0.Co;2), 1992.

767 Che, H. Z., Gui, K., Xia, X. G., Wang, Y. Q., Holben, B. N., Goloub, P., Cuevas-Agullo, E., Wang,
768 H., Zheng, Y., Zhao, H. J., and Zhang, X. Y.: Large contribution of meteorological factors to inter-
769 decadal changes in regional aerosol optical depth, *Atmos. Chem. Phys.*, 19, 10497-10523,
770 <https://doi.org/10.5194/acp-19-10497-2019>, 2019.

771 Chen, S. Y., Huang, J. P., Kang, L. T., Wang, H., Ma, X. J., He, Y. L., Yuan, T. G., Yang, B., Huang,
772 Z. W., and Zhang, G. L.: Emission, transport, and radiative effects of mineral dust from the



- 773 Taklimakan and Gobi deserts: comparison of measurements and model results, *Atmos. Chem.*
774 *Phys.*, 17, 2401-2421, <https://doi.org/10.5194/acp-17-2401-2017>, 2017.
- 775 Chiapello, I., Moulin, C., and Prospero, J. M.: Understanding the long-term variability of African
776 dust transport across the Atlantic as recorded in both Barbados surface concentrations and large-
777 scale Total Ozone Mapping Spectrometer (TOMS) optical thickness, *J. Geophys. Res.-Atmos.*,
778 110, 9, <https://doi.org/10.1029/2004jd005132>, 2005.
- 779 Czaja, A. and Frankignoul, C.: Observed Impact of Atlantic SST Anomalies on the North Atlantic
780 Oscillation, *J. Clim.*, 15, 606-623, [https://doi.org/10.1175/1520-0442\(2002\)015<0606:Oioasa>2.0.Co;2](https://doi.org/10.1175/1520-0442(2002)015<0606:Oioasa>2.0.Co;2), 2002.
- 782 Duce, R. A., Unni, C. K., Ray, B. J., Prospero, J. M., and Merrill, J. T.: Long-Range Atmospheric
783 Transport of Soil Dust from Asia to the Tropical North Pacific: Temporal Variability, *Science*,
784 209, 1522-1524, <https://doi.org/10.1126/science.209.4464.1522>, 1980.
- 785 Feng, J., Li, J. P., Liao, H., and Zhu, J. L.: Simulated coordinated impacts of the previous autumn
786 North Atlantic Oscillation (NAO) and winter El Nino on winter aerosol concentrations over
787 eastern China, *Atmos. Chem. Phys.*, 19, 10787-10800, [https://doi.org/10.5194/acp-19-10787-](https://doi.org/10.5194/acp-19-10787-2019)
788 2019, 2019.
- 789 Feng, J., Zhu, J. L., Li, J. P., and Liao, H.: Aerosol concentrations variability over China: two distinct
790 leading modes, *Atmos. Chem. Phys.*, 20, 9883-9893, <https://doi.org/10.5194/acp-20-9883-2020>,
791 2020.
- 792 Gary, L.: *Midlatitude Synoptic Meteorology Dynamics, Analysis, and Forecasting*, American
793 Meteorological Society, American, 2012.
- 794 Gelaro, R., McCarty, W., Suarez, M. J., Todling, R., Molod, A., Takacs, L., Randles, C. A.,
795 Darmenov, A., Bosilovich, M. G., Reichle, R., Wargan, K., Coy, L., Cullather, R., Draper, C.,
796 Akella, S., Buchard, V., Conaty, A., da Silva, A. M., Gu, W., Kim, G. K., Koster, R., Lucchesi, R.,
797 Merkova, D., Nielsen, J. E., Partyka, G., Pawson, S., Putman, W., Rienecker, M., Schubert, S. D.,
798 Sienkiewicz, M., and Zhao, B.: The Modern-Era Retrospective Analysis for Research and
799 Applications, Version 2 (MERRA-2), *J. Clim.*, 30, 5419-5454, [https://doi.org/10.1175/jcli-d-16-](https://doi.org/10.1175/jcli-d-16-0758.1)
800 0758.1, 2017.
- 801 Giannini, A., Kushnir, Y., and Cane, M. A.: Interannual variability of Caribbean rainfall, ENSO, and



802 the Atlantic Ocean, *J. Clim.*, 13, 297-311, <https://doi.org/10.1175/1520->
803 0442(2000)013<0297:Ivocre>2.0.Co;2, 2000.

804 Ginoux, P., Prospero, J. M., Torres, O., and Chin, M.: Long-term simulation of global dust
805 distribution with the GOCART model: correlation with North Atlantic Oscillation, *Environ.*
806 *Modell. Softw.*, 19, 113-128, [https://doi.org/10.1016/s1364-8152\(03\)00114-2](https://doi.org/10.1016/s1364-8152(03)00114-2), 2004.

807 Ginoux, P., Prospero, J. M., Gill, T. E., Hsu, N. C., and Zhao, M.: Global-scale attribution of
808 anthropogenic and natural dust sources and their emission rates based on MODIS Deep Blue
809 aerosol products, *Rev. Geophys.*, 50, 36, <https://doi.org/10.1029/2012rg000388>, 2012.

810 Graf, H.-F. and Zanchettin, D.: Central Pacific El Niño, the “subtropical bridge,” and Eurasian
811 climate, *J. Geophys. Res.-Atmos.*, 117, <https://doi.org/10.1029/2011JD016493>, 2012.

812 Han, Y., Wang, T. H., Tang, J. Y., Wang, C. Y., Jian, B. D., Huang, Z. W., and Huang, J. P.: New
813 insights into the Asian dust cycle derived from CALIPSO lidar measurements, *Remote Sens.*
814 *Environ.*, 272, 15, <https://doi.org/10.1016/j.rse.2022.112906>, 2022.

815 Hartley, S. and Keables, M. J.: Synoptic associations of winter climate and snowfall variability in
816 New England, USA, 1950-1992, *Int. J. Climatol.*, 18, 281-298,
817 [https://doi.org/10.1002/\(sici\)1097-0088\(19980315\)18:3<281::Aid-joc245>3.0.Co;2-f](https://doi.org/10.1002/(sici)1097-0088(19980315)18:3<281::Aid-joc245>3.0.Co;2-f), 1998.

818 Holopainen, E. O. and Oort, A. H.: On the Role of Large-Scale Transient Eddies in the Maintenance
819 of the Vorticity and Enstrophy of the Time-Mean Atmospheric Flow, *J. Atmos. Sci.*, 38, 270-280,
820 [https://doi.org/10.1175/1520-0469\(1981\)038<0270:Otrots>2.0.Co;2](https://doi.org/10.1175/1520-0469(1981)038<0270:Otrots>2.0.Co;2), 1981.

821 Holopainen, E. O., Rontu, L., and Lau, N. C.: The Effect of Large-Scale Transient Eddies on the
822 Time-Mean Flow in the Atmosphere, *J. Atmos. Sci.*, 39, 1972-1984,
823 [https://doi.org/10.1175/1520-0469\(1982\)039<1972:Teolst>2.0.Co;2](https://doi.org/10.1175/1520-0469(1982)039<1972:Teolst>2.0.Co;2), 1982.

824 Hong, S. K., Ryoo, S. B., Kim, J., and Lee, S. S.: Prediction of Asian Dust Days over Northern
825 China Using the KMA-ADAM2 Model, *Weather Forecast.*, 34, 1777-1787,
826 <https://doi.org/10.1175/waf-d-19-0008.1>, 2019.

827 Huang, B. Y., Thorne, P. W., Banzon, V. F., Boyer, T., Chepurin, G., Lawrimore, J. H., Menne, M.
828 J., Smith, T. M., Vose, R. S., and Zhang, H. M.: Extended Reconstructed Sea Surface Temperature,
829 Version 5 (ERSSTv5): Upgrades, Validations, and Intercomparisons, *J. Clim.*, 30, 8179-8205,
830 <https://doi.org/10.1175/jcli-d-16-0836.1>, 2017.



- 831 Huang, J. P., Liu, J. J., Chen, B., and Nasiri, S. L.: Detection of anthropogenic dust using CALIPSO
832 lidar measurements, *Atmos. Chem. Phys.*, 15, 11653-11665, [https://doi.org/10.5194/acp-15-](https://doi.org/10.5194/acp-15-11653-2015)
833 11653-2015, 2015.
- 834 Huang, J. P., Wang, T. H., Wang, W. C., Li, Z. Q., and Yan, H. R.: Climate effects of dust aerosols
835 over East Asian arid and semiarid regions, *J. Geophys. Res.-Atmos.*, 119, 11398-11416,
836 <https://doi.org/10.1002/2014jd021796>, 2014a.
- 837 Huang, J. P., Lin, B., Minnis, P., Wang, T. H., Wang, X., Hu, Y. X., Yi, Y. H., and Ayers, J. K.:
838 Satellite-based assessment of possible dust aerosols semi-direct effect on cloud water path over
839 East Asia, *Geophys. Res. Lett.*, 33, 5, <https://doi.org/10.1029/2006gl026561>, 2006.
- 840 Huang, X., Song, Y., Zhao, C., Li, M. M., Zhu, T., Zhang, Q., and Zhang, X. Y.: Pathways of sulfate
841 enhancement by natural and anthropogenic mineral aerosols in China, *J. Geophys. Res.-Atmos.*,
842 119, 14165-14179, <https://doi.org/10.1002/2014jd022301>, 2014b.
- 843 Huang, Y. H., Liu, X. D., Yin, Z. Y., and An, Z. S.: Global Impact of ENSO on Dust Activities with
844 Emphasis on the Key Region from the Arabian Peninsula to Central Asia, *J. Geophys. Res.-*
845 *Atmos.*, 126, 24, <https://doi.org/10.1029/2020jd034068>, 2021.
- 846 Hurrell, J. W.: Decadal Trends in the North Atlantic Oscillation: Regional Temperatures and
847 Precipitation, *Science*, 269, 676-679, <https://doi.org/10.1126/science.269.5224.676>, 1995.
- 848 Jin, F. F., Pan, L. L., and Watanabe, M.: Dynamics of synoptic eddy and low-frequency flow
849 interaction. Part I: A linear closure, *J. Atmos. Sci.*, 63, 1677-1694,
850 <https://doi.org/10.1175/jas3715.1>, 2006.
- 851 Jin, Q. J., Yang, Z. L., and Wei, J. F.: Seasonal Responses of Indian Summer Monsoon to Dust
852 Aerosols in the Middle East, India, and China, *J. Clim.*, 29, 6329-6349,
853 <https://doi.org/10.1175/jcli-d-15-0622.1>, 2016.
- 854 Kang, L. T., Huang, J. P., Chen, S. Y., and Wang, X.: Long-term trends of dust events over Tibetan
855 Plateau during 1961-2010, *Atmos. Environ.*, 125, 188-198,
856 <https://doi.org/10.1016/j.atmosenv.2015.10.085>, 2016.
- 857 Kaufman, Y. J., Tanre, D., and Boucher, O.: A satellite view of aerosols in the climate system, *Nature*,
858 419, 215-223, <https://doi.org/10.1038/nature01091>, 2002.
- 859 Kleist, D. T., Parrish, D. F., Derber, J. C., Treadon, R., Errico, R. M., and Yang, R. H.: Improving



- 860 Incremental Balance in the GSI 3DVAR Analysis System, *Mon. Weather Rev.*, 137, 1046-1060,
861 <https://doi.org/10.1175/2008mwr2623.1>, 2009.
- 862 Kutiel, H. and Furman, H.: Dust storms in the Middle East: Sources of origin and their temporal
863 characteristics, *Indoor Built Environ.*, 12, 419-426, <https://doi.org/10.1177/1420326x03037110>,
864 2003.
- 865 Lau, N. C. and Nath, M. J.: Variability of the Baroclinic and Barotropic Transient Eddy Forcing
866 Associated with Monthly Changes in the Midlatitude Storm Tracks, *J. Atmos. Sci.*, 48, 2589-2613,
867 [https://doi.org/10.1175/1520-0469\(1991\)048<2589:Votbab>2.0.Co;2](https://doi.org/10.1175/1520-0469(1991)048<2589:Votbab>2.0.Co;2), 1991.
- 868 Li, J., Garshick, E., Huang, S. D., and Koutrakis, P.: Impacts of El Nino-Southern Oscillation on
869 surface dust levels across the world during 1982-2019, *Sci. Total Environ.*, 769, 7,
870 <https://doi.org/10.1016/j.scitotenv.2020.144566>, 2021b.
- 871 Li, J. P. and Wang, J. X. L.: A new North Atlantic Oscillation index and its variability, *Adv. Atmos.*
872 *Sci.*, 20, 661-676, <https://doi.org/10.1007/BF02915394>, 2003.
- 873 Li, J. P., Zheng, F., Sun, C., Feng, J., and Wang, J.: Pathways of Influence of the Northern
874 Hemisphere Mid-high Latitudes on East Asian Climate: A Review, *Adv. Atmos. Sci.*, 36, 902-921,
875 <https://doi.org/10.1007/s00376-019-8236-5>, 2019a.
- 876 Li, M. Y., Yao, Y., Simmonds, I., Luo, D. H., Zhong, L. H., and Pei, L.: Linkages between the
877 atmospheric transmission originating from the North Atlantic Oscillation and persistent winter
878 haze over Beijing, *Atmos. Chem. Phys.*, 21, 18573-18588, [https://doi.org/10.5194/acp-21-18573-](https://doi.org/10.5194/acp-21-18573-2021)
879 2021, 2021a.
- 880 Li, X., Liu, X. D.: Relation of Spring Dust-Storm Activities in Northern China and Changes of
881 Upper Westerlies, *Plateau. Meteorology (in Chinese)*, 34, 1292-1300,
882 <https://doi.org/10.7522/j.issn.1000-0534.2014.00067>, 2015.
- 883 Li, Y., Lu, Y., and Wang, C. H.: Characteristics of thermal and momentum transport during the
884 lifetime of Ural blocking highs, *Int. J. Climatol.*, 40, 77-93, <https://doi.org/10.1002/joc.6195>,
885 2019c.
- 886 Li, Y., Hu, X. L., Wang, X., and Ji, M. X.: Impact of transient eddy fluxes on the dust storm event:
887 Cases study in South Xinjiang, China, *Atmos. Res.*, 269, 11,
888 <https://doi.org/10.1016/j.atmosres.2022.106054>, 2022.



- 889 Li, Y., Zhang, J. Y., Lu, Y., Zhu, J. L., and Feng, J.: Characteristics of Transient Eddy Fluxes during
890 Blocking Highs Associated with Two Cold Events in China, *Atmosphere*, 10, 15,
891 <https://doi.org/10.3390/atmos10050235>, 2019b.
- 892 Lin, H. and Wu, Z. W.: Contribution of the Autumn Tibetan Plateau Snow Cover to Seasonal
893 Prediction of North American Winter Temperature, *J. Clim.*, 24, 2801-2813,
894 <https://doi.org/10.1175/2010jcli3889.1>, 2011.
- 895 Liu, J., Wu, D. Y., Liu, G. J., Mao, R., Chen, S. Y., Ji, M. X., Fu, P. Q., Sun, Y. L., Pan, X. L., Jin,
896 H. C., Zhou, Y. B., and Wang, X.: Impact of Arctic amplification on declining spring dust events
897 in East Asia, *Clim. Dyn.*, 54, 1913-1935, <https://doi.org/10.1007/s00382-019-05094-4>, 2020.
- 898 Liu, X. D. and Yin, Z. Y.: Spatial and temporal variation of summer precipitation over the eastern
899 Tibetan Plateau and the North Atlantic oscillation, *J. Clim.*, 14, 2896-2909,
900 [https://doi.org/10.1175/1520-0442\(2001\)014<2896:Satvos>2.0.Co;2](https://doi.org/10.1175/1520-0442(2001)014<2896:Satvos>2.0.Co;2), 2001.
- 901 Liu, X. D., Yin, Z. Y., Zhang, X. Y., and Yang, X. C.: Analyses of the spring dust storm frequency
902 of northern China in relation to antecedent and concurrent wind, precipitation, vegetation, and
903 soil moisture conditions, *J. Geophys. Res.-Atmos.*, 109, 16,
904 <https://doi.org/10.1029/2004jd004615>, 2004.
- 905 Mao, R., Ho, C. H., Shao, Y., Gong, D. Y., and Kim, J.: Influence of Arctic Oscillation on dust
906 activity over northeast Asia, *Atmos. Environ.*, 45, 326-337,
907 <https://doi.org/10.1016/j.atmosenv.2010.10.020>, 2011.
- 908 Molod, A., Takacs, L., Suarez, M., and Bacmeister, J.: Development of the GEOS-5 atmospheric
909 general circulation model: evolution from MERRA to MERRA2, *Geosci. Model Dev.*, 8, 1339-
910 1356, <https://doi.org/10.5194/gmd-8-1339-2015>, 2015.
- 911 Nie, W., Ding, A. J., Wang, T., Kerminen, V. M., George, C., Xue, L. K., Wang, W. X., Zhang Q.
912 Z., Petaja, T., Qi, X. M., Gao, X. M., Wang, X. F., Yang, X. Q., Fu, C. B., and Kulmala, M.:
913 Polluted dust promotes new particle formation and growth, *Sci Rep*, 4, 6634,
914 <https://doi.org/10.1038/srep08949>, 2015.
- 915 Qian, W. H.: Physical decomposition principle of regional-scale atmospheric transient anomaly, *J.*
916 *Geophys (in Chinese)*., 55, 1439-1448, <https://doi.org/10.6038/j.issn.0001-5733.2012.05.002>,
917 2012.



- 918 Qian, W. H., Quan, L. S., and Shi, S. Y.: Variations of the dust storm in China and its climatic control,
919 J. Clim., 15, 1216-1229, [10.1175/1520-0442\(2002\)015<1216:Votdsi>2.0.Co;2](https://doi.org/10.1175/1520-0442(2002)015<1216:Votdsi>2.0.Co;2), 2002.
- 920 Sassen, K., DeMott, P. J., Prospero, J. M., and Poellot, M. R.: Saharan dust storms and indirect
921 aerosol effects on clouds: CRYSTAL-FACE results, Geophys. Res. Lett., 30,
922 <https://doi.org/10.1029/2003GL017371>, 2003.
- 923 Shao, T. H., Zhang, Y. C.: Influence of Winter North Atlantic Oscillation on Spring Precipitation in
924 China, Plateau. Meteorology (in Chinese)., 31, 1225-1233,
925 <https://doi.org/CNKI:SUN:GYQX.0.2012-05-006>, 2012.
- 926 Shao, Y. P., Yang, Y., Wang, J. J., Song, Z. X., Leslie, L. M., Dong, C. H., Zhang, Z. H., Lin, Z. H.,
927 Kanai, Y., Yabuki, S., and Chun, Y. S.: Northeast Asian dust storms: Real-time numerical
928 prediction and validation, J. Geophys. Res.-Atmos., 108, 18,
929 <https://doi.org/10.1029/2003jd003667>, 2003.
- 930 Sokolik, I. N. and Toon, O. B.: Direct radiative forcing by anthropogenic airborne mineral aerosols,
931 Nature, 381, 681-683, <https://doi.org/10.1038/381681a0>, 1996.
- 932 Solomon, A. B.: An observational study of the spatial and temporal scales of transient eddy sensible
933 heat fluxes, J. Clim., 10, 508-520, [https://doi.org/10.1175/1520-0442\(1997\)010<0508:Aosots>2.0.Co;2](https://doi.org/10.1175/1520-0442(1997)010<0508:Aosots>2.0.Co;2), 1997.
- 935 Tang, H. Y., Zhai, P. M., and Chang, Y. K.: SVD Analysis between Northern Hemisphere 500 hPa
936 Heights and Spring Duststorms over Northern China, J. Dersert. Res (in Chinese)., 25, 570-576,
937 <https://doi.org/10.3321/j.issn:1000-694X.2005.04.020>, 2005.
- 938 Trenberth, K. E.: An assessment of the impact of transient eddies on the zonal flow during a blocking
939 episode using localized Eliassen-Palm flux diagnostics, J. Atmos. Sci., 43, 2070-2087,
940 [https://doi.org/10.1175/1520-0469\(1986\)043<2070:Aaotio>2.0.Co;2](https://doi.org/10.1175/1520-0469(1986)043<2070:Aaotio>2.0.Co;2), 1986.
- 941 Walker, G. T.: Correlations in seasonal variations of weather IX, Indian Meteor. Dept., 24, 275-332,
942 1924.
- 943 Wang, X., Liu, J., Che, H. Z., Ji, F., and Liu, J. J.: Spatial and temporal evolution of natural and
944 anthropogenic dust events over northern China, Sci Rep, 8, 2141, <https://doi.org/10.1038/s41598-018-20382-5>, 2018.
- 946 Wang, X. M., Zhai, P. M., and Wang, C. C.: Variations in extratropical cyclone activity in northern



- 947 East Asia, *Adv. Atmos. Sci.*, 26, 471-479, <https://doi.org/10.1007/s00376-009-0471-8>, 2009.
- 948 Wang, Y. B., Shi, N.: Relation of North Atlantic Oscillation Anomaly to China Climate during 1951-
949 1995, *Trans. Atmos. Sci. (in Chinese)*, 24, 315-322, <https://doi.org/10.3969/j.issn.1674-7097.2001.03.003>, 2001.
- 951 Washington, R., Todd, M., Middleton, N. J., and Goudie, A. S.: Dust-storm source areas determined
952 by the total ozone monitoring spectrometer and surface observations, *Ann. Assoc. Am. Geogr.*,
953 93, 297-313, <https://doi.org/10.1111/1467-8306.9302003>, 2003.
- 954 Watanabe, M.: Asian jet waveguide and a downstream extension of the North Atlantic Oscillation,
955 *J. Clim.*, 17, 4674-4691, <https://doi.org/10.1175/jcli-3228.1>, 2004.
- 956 Watanabe, M. and Kimoto, M.: Atmosphere-ocean thermal coupling in the North Atlantic: A
957 positive feedback, *Q. J. R. Meteorol. Soc.*, 126, 3343-3369, <https://doi.org/10.1002/qj.49712657017>, 2000.
- 959 Wilcox, L. J., Liu, Z., Samset, B. H., Hawkins, E., Lund, M. T., Nordling, K., Undorf, S., Bollasina,
960 M., Ekman, A. M. L., Krishnan, S., Merikanto, J., and Turner, A. G.: Accelerated increases in
961 global and Asian summer monsoon precipitation from future aerosol reductions, *Atmospheric
962 Chemistry and Physics*, 20, 11955-11977, [10.5194/acp-20-11955-2020](https://doi.org/10.5194/acp-20-11955-2020), 2020.
- 963 Wu, J., Kurosaki, Y., Shinoda, M., and Kai, K. J.: Regional Characteristics of Recent Dust
964 Occurrence and Its Controlling Factors in East Asia, *Sola*, 12, 187-191,
965 <https://doi.org/10.2151/sola.2016-038>, 2016.
- 966 Wu, Z. X., Wang, S. G., Shang, K. Z., Yang, Z. F., and Chen, F.: The characteristics of momentum
967 transfer during a cold strong wind process. *J. Desert. Res (in Chinese)*, 36, 467-473,
968 <https://doi.org/10.7522/j.issn.1000-694X.2015.00134>, 2016.
- 969 Wu, Z. W., Wang, B., Li, J. P., and Jin, F. F.: An empirical seasonal prediction model of the east
970 Asian summer monsoon using ENSO and NAO, *J. Geophys. Res.-Atmos.*, 114, 13,
971 <https://doi.org/10.1029/2009jd011733>, 2009.
- 972 Xuan, J., Liu, G. L., and Du, K.: Dust emission inventory in Northern China, *Atmos. Environ.*, 34,
973 4565-4570, [https://doi.org/10.1016/s1352-2310\(00\)00203-x](https://doi.org/10.1016/s1352-2310(00)00203-x), 2000.
- 974 Yang, Y., Zeng, L., Wang, H., Wang, P., and Liao, H.: Dust pollution in China affected by different
975 spatial and temporal types of El Niño, *Atmos. Chem. Phys.*, 22, 14489-14502,



- 976 <https://doi.org/10.5194/acp-22-14489-2022>, 2022.
- 977 Yao, W. R., Gui, K., Wang, Y. Q., Che, H. Z., and Zhang, X. Y.: Identifying the dominant local
978 factors of 2000-2019 changes in dust loading over East Asia, *Sci. Total Environ.*, 777, 10,
979 <https://doi.org/10.1016/j.scitotenv.2021.146064>, 2021.
- 980 Yao, Y., Zhang, W. Q., Luo, D. H., Zhong, L. H., and Pei, L.: Seasonal Cumulative Effect of Ural
981 Blocking Episodes on the Frequent Cold events in China during the Early Winter of 2020/21,
982 *Adv. Atmos. Sci.*, 39, 609-624, <https://doi.org/10.1007/s00376-021-1100-4>, 2022.
- 983 Yin, Z. C., Wan, Y., Zhang, Y. J., and Wang, H. J.: Why super sandstorm 2021 in North China?, *Natl.*
984 *Sci. Rev.*, 9, 9, <https://doi.org/10.1093/nsr/nwab165>, 2021.
- 985 Yu, B., Lin, H., Wu, Z. W., and Merryfield, W. J.: Relationship between North American winter
986 temperature and large-scale atmospheric circulation anomalies and its decadal variation, *Environ.*
987 *Res. Lett.*, 11, 8, <https://doi.org/10.1088/1748-9326/11/7/074001>, 2016.
- 988 Yu, X. C., Wang, Z. L., Zhang, H., and Zhao, S. Y.: Impacts of different types and intensities of El
989 Niño events on winter aerosols over China, *Sci. Total Environ.*, 655, 766-780,
990 [10.1016/j.scitotenv.2018.11.090](https://doi.org/10.1016/j.scitotenv.2018.11.090), 2019.
- 991 Zender, C. S., Miller, R. L., and Tegen, I.: Quantifying mineral dust mass budgets: Terminology,
992 constraints, and current estimates, *Eos, Transactions American Geophysical Union*, 85, 509-512,
993 <https://doi.org/10.1029/2004EO480002>, 2004.
- 994 Zhang, C. X., Liu, C., Hu, Q. H., Cai, Z. N., Su, W. J., Xia, C. Z., Zhu, Y. Z., Wang, S. W., and Liu,
995 J. G.: Satellite UV-Vis spectroscopy: implications for air quality trends and their driving forces
996 in China during 2005-2017, *Light-Sci. Appl.*, 8, 12, <https://doi.org/10.1038/s41377-019-0210-6>,
997 2019.
- 998 Zhang, L., Zhang, H. S., Li, Q. H., Cai, X. H., and Song, Y.: Vertical dispersion mechanism of long-
999 range transported dust in Beijing: Effects of atmospheric turbulence, *Atmos. Res.*, 269, 12,
1000 <https://doi.org/10.1016/j.atmosres.2022.106033>, 2022.
- 1001 Zhang, P., Wu, Z. W., and Jin, R.: How can the winter North Atlantic Oscillation influence the early
1002 summer precipitation in Northeast Asia: effect of the Arctic sea ice, *Clim. Dyn.*, 56, 1989-2005,
1003 <https://doi.org/10.1007/s00382-020-05570-2>, 2021.
- 1004 Zhang, W. J., Wang, L., Xiang, B. Q., Qi, L., and He, J. H.: Impacts of two types of La Nina on the



- 1005 NAO during boreal winter, *Clim. Dyn.*, 44, 1351-1366, <https://doi.org/10.1007/s00382-014->
1006 2155-z, 2015.
- 1007 Zhang, X. Y., Arimoto, R., and An, Z. S.: Dust emission from Chinese desert sources linked to
1008 variations in atmospheric circulation, *J. Geophys. Res.-Atmos.*, 102, 28041-28047,
1009 <https://doi.org/10.1029/97jd02300>, 1997.
- 1010 Zhang, X. Y., Gong, S. L., Zhao, T. L., Arimoto, R., Wang, Y. Q., and Zhou, Z. J.: Sources of Asian
1011 dust and role of climate change versus desertification in Asian dust emission, *Geophys. Res. Lett.*,
1012 30, 4, <https://doi.org/10.1029/2003gl018206>, 2003.
- 1013 Zhang, X. Y., Wang, Y. Q., Niu, T., Zhang, X. C., Gong, S. L., Zhang, Y. M., and Sun, J. Y.:
1014 Atmospheric aerosol compositions in China: spatial/temporal variability, chemical signature,
1015 regional haze distribution and comparisons with global aerosols, *Atmos. Chem. Phys.*, 12, 6273-
1016 6273, <https://doi.org/10.5194/acp-12-6273-2012>, 2012.
- 1017 Zhao, S., Li, J. P., and Sun, C.: Decadal variability in the occurrence of wintertime haze in central
1018 eastern China tied to the Pacific Decadal Oscillation, *Sci Rep*, 6, 9,
1019 <https://doi.org/10.1038/srep27424>, 2016.
- 1020 Zhao, Y., Li, H. J., and He, Q.: Variation of dust storm days in Tarim Basin and its relation with
1021 North Atlantic Oscillation, *J. Desert. Res (in Chinese)*, 32, 1082-1088, <https://doi.org/>
1022 CNKI:SUN:ZGSS.0.2012-04-027, 2012.
1023